The Pennsylvania State University

The Graduate School

Department of Electrical Engineering

LOW-LOSS DISPERSION ENGINEERED WIDE-BAND, MULTI-BAND, AND RECONFIGURABLE ANISOTROPIC METAMATERIALS AND BÉZIER METASURFACES

A Dissertation in

Electrical Engineering

by

Peter E. Sieber

Submitted in Partial Fulfillment
of the Requirements
for the Degree of

Doctor of Philosophy

August 2015

The dissertation of Peter E. Sieber was reviewed and approved* by the following:

Douglas H. Werner
Professor of Electrical Engineering
Dissertation Advisor
Chair of Committee

Theresa S. Mayer
Professor of Electrical Engineering
Associate Dean for Research and Innovation

David C. Swanson
Senior Research Associate and Associate Professor of Acoustics

Pingjiuan L. Werner
Professor of Electrical Engineering

Kultegin Aydin
Professor of Electrical Engineering
Head of the Department of Electrical Engineering

*Signatures are on file in the Graduate School

ABSTRACT

For more than a decade, metamaterials have generated significant interest due to their theoretical and later experimentally demonstrated properties that are not observed in nature; yet, many of these designs are plagued by very limited bandwidth and/or high losses due to the dispersion characteristics of metamaterials. While many applications exist where a narrow band response is acceptable, examples of dual-band and multi-band responses within a communication bandwidth are limited. Furthermore, the ability to implement reconfigurability becomes complicated due to the lack of high performance switch technologies. In this dissertation, a new technique for constructing and synthesizing broadband metasurfaces is presented. A synthesis technique using Bézier surfaces is subsequently shown to not only outperform known optimization techniques but to produce results with bandwidths far exceeding those found in the literature. Additionally, a composite metamaterial geometry is introduced that facilitates a dual band response with a tunable frequency ratio within usable bands. The design also facilitates reconfigurablity. To mitigate the loss and bandwidth concerns of existing RF switch technologies a new technology is introduced and characterized - a chalcogenide glass phase change material enabled bistable switch. The superior efficiency and bandwidth are subsequently demonstrated by a novel quad state frequency selective surface, which once again boasts multiband reconfigurability within a communication band.

TABLE OF CONTENTS

LIST OF FIGURES

Chapter 1

Introduction

Since their inception almost two decades ago, metamaterials have generated significant interest due to their theoretically [1-6] and later experimentally [7-10] demonstrated properties which are not observed in naturally occurring materials. Such early examples include negative permeability, left-handed media, cloaks of invisibility and perfect lenses [1-10]. Metamaterials derive their unique properties from engineered electromagnetic responses, most often in the form of 2-D and 3D periodic arrays of metallic unit-cells, which, in order to avoid grating lobes at oblique incidence, are smaller than their operational wavelength [11]. As such, these sub-wavelength metamaterial unit-cells are analogous to atoms in a crystal lattice. Yet, metamaterial unit-cells differ from atoms in that in order to achieve a bulk response; they only need to be slightly smaller than their operational wavelength, resulting in realizable fabrication dimensions well into the optical range.

Naturally occurring materials exhibit electrical conduction that is dictated by the transport of its electrons. In the classical sense, this behavior can be described in terms of a superposition of second-order Lorentzian (resonant) functions [12]. In its simplest form, the relative permittivity of a lossless material as a function of angular frequency can be modeled by the Lorentz-Drude model [12],

$$\varepsilon'(\omega) = \left(1 - \frac{\omega_p^2}{\omega^2}\right), \tag{1.1}$$

where ω_p represents the plasma frequency. In a naturally occurring material, the plasma frequency can be solved for directly using solid state physics, where the plasma frequency is defined as a function of the electron density, N, the electron charge, q, the electron mass, m, and free space permittivity, ε_0, as [12]

$$\omega_p = \sqrt{\frac{Nq^2}{m\varepsilon_0}}. \tag{1.2}$$

Applying effective medium theory to metallo-dielectric metamaterials, the same dispersive Lorentz-Drude model applies. An effective electron density, electron charge, and effective electron mass can be determined for specific metamaterial geometries [13].

The total energy in a non-dispersive medium is given as the sum of the electric and magnetic energies [14]

$$U_{total} = \frac{1}{4}\varepsilon|\boldsymbol{E}|^2 + \frac{1}{4}\mu|\boldsymbol{H}|^2.$$

(1.3)

However, in order to account for resonances, naturally occurring or engineered, the medium must exhibit dispersive material parameters, such that

$$U_{total} = \frac{1}{4}\frac{\partial\varepsilon(\omega)}{\partial\omega}|\boldsymbol{E}|^2 + \frac{1}{4}\frac{\partial\mu(\omega)}{\partial\omega}|\boldsymbol{H}|^2,$$

(1.4)

where, even for the cases of negative permittivity and permeability, their respective derivatives are always positive due to energy conservation [14]. Ignoring loss, the dispersive behavior of a metamaterial can be expressed in terms of the real parts of its constituent parameters as [14]

$$Re[\varepsilon_r(\omega)] = \varepsilon_r'(\omega) = 1 - \frac{\omega_{p,e}^2}{\omega^2 - \omega_{0,e}^2}$$

(1.5)

and

$$Re[\mu_r(\omega)] = \mu_r'(\omega) = 1 - \frac{\omega_{p,m}^2}{\omega^2 - \omega_{0,m}^2},$$

(1.6)

where $\omega_{p,e}$ and $\omega_{p,m}$ are the electric and magnetic plasma frequencies and $\omega_{0,e}$ and $\omega_{0,m}$ are the electric and magnetic resonant frequencies, respectively.

Introducing loss, the Kramers-Kronig equations relate the real part of the constituent parameters to their imaginary parts (loss) as follows

$$\varepsilon_r'(\omega) = 1 + \frac{2}{\pi}\int_0^{\infty} \frac{\omega'\varepsilon_r''(\omega')}{(\omega')^2 - \omega^2} d\omega'$$

(1.7)

and

$$\varepsilon_r''(\omega) = \frac{2\omega}{\pi}\int_0^{\infty} \frac{1 - \varepsilon_r'(\omega)}{(\omega')^2 - \omega^2} d\omega'$$

(1.8)

where the real and imaginary permeabilies can be expressed in an identical fashion [15].

From the Kramers-Kronig equations it is apparent that a large increase or decrease in permittivity corresponds to a large increase in loss. Refining Equation 1.4 and Equation 1.5, loss can be accounted for through the addition of a dampening coefficient, Γ, as follows

$$\varepsilon_r(\omega) = \varepsilon_r'(\omega) + j\varepsilon_r''(\omega) = 1 - \frac{\omega_{p,e}^2}{\left(\omega^2 - \omega_{0,e}^2\right) + j\omega\Gamma(\omega)}.$$

(1.9)

This dispersive dampening coefficient takes into account all system losses, consisting of conductor losses, dielectric losses, and radiation losses.

In order to gain further insight into a material's dispersive behavior, it is convenient to first characterize the dispersive behavior of metallo-dielectric metamaterials in terms of an equivalent circuit defined in terms of resistance, inductance and capacitance (RLC). First and foremost, the resonance frequency is given as

$$\omega_0 = \frac{1}{\sqrt{LC}} \tag{1.10}$$

while the aforementioned system loss is expressed in terms of total resistance as [16]

$$R_{total} = R_c + R_d + R_r. \tag{1.11}$$

Generally speaking, especially for radio frequencies (RF), the conductor (R_c), and dielectric (R_d) resistances are minimized through the use of highly conductive metals and low-loss dielectrics. As such, the metamaterial losses are dominated by the radiation resistance, R_r. For the specific case of a split-ring resonator (SRR) [2], the radiation resistance as a function of unit-cell size, relative to wavelength, is plotted in Figure 1.1. From Figure 1.1, we can observe that the SRR becomes more resistive due to increased radiation losses as the unit-cell size increases; similarly, and perhaps more intuitively, this can also be described as an antenna's radiating efficiency increasing as its size approaches its operating frequency.

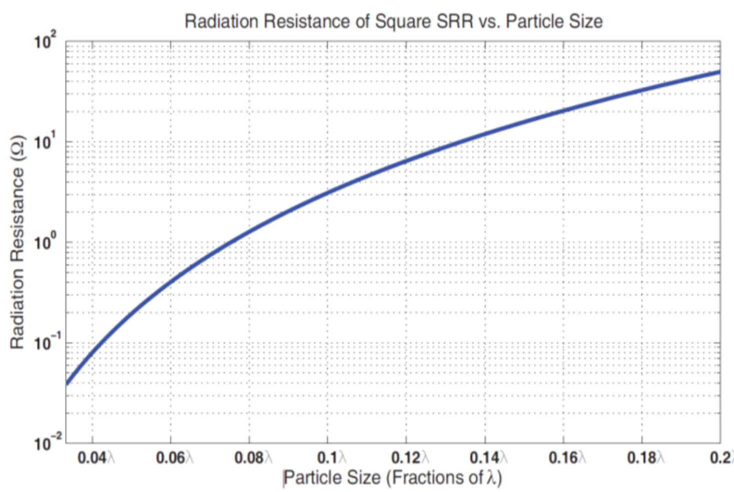

Figure 1.1. Radiation resistance of a SRR as a function of unit-cell size relative to wavelength [16].

The relation of stored energy (LC) to loss (R_{total}) is quantified by the quality (Q) factor. The Q-factor is defined in terms of reactance (X), angular frequency (ω), and loss as [17]

$$Q = \frac{\omega_0}{2R_{total}}\left|\frac{\partial X}{\partial \omega}\right|. \tag{1.12}$$

From this expression the dispersion or more specifically, the rate of change of the surface impedance as a function of frequency, can be related to the Q-factor as

$$\left|\frac{\partial X}{\partial \omega}\right| \propto Q \propto \frac{1}{B},$$

(1.13)

where the bandwidth (B) shares an inversely proportional relationship with the Q-factor and surface impedance dispersion.

1.1 Statement of Problem

The insight gained from the two expressions in Equations 1.13 and 1.14 can be used to underscore two fundamental limitations in metamaterial applications. First, operational bandwidths are fundamentally limited by the high Q-factors that metamaterials exhibit due to the requirement of sub-wavelength unit-cell dimensions. As such, the dispersion can only be moderately decreased through lowering the Q-factor. Thus, a need remains to develop techniques to design broadband metamaterials which are compatible with existing communication bands. This is discussed further in Section 1.2.1.

Conversely, as is the case for many multi-band designs, the Q-factor is generally maximized to facilitate multiple resonant frequencies within a desired frequency bandwidth. The challenge then becomes how to design multiple resonances within a small bandwidth. This becomes especially challenging when one is restricted to using only one metallic layer. As such, a need to develop an intuitive approach towards dual band reconfigurability especially in the context of antennas is needed. This is discussed in greater detail in Section 1.2.2.

Likewise, for reconfigurable designs, a narrow bandwidth, high Q response is also desirable, allowing for a discernible shift between states. In practice, insertion loss of commonly used switches can compromise the metamaterial Q-factor due to significantly increased losses resulting from impedance mismatching and ohmic losses. Furthermore, the capacitance of the switch ultimately limits the upper operating frequency by degrading the off-state resistance. Thus, there is a need to address loss and operating frequency limitations in the context of reconfigurable metamaterial designs. This is discussed in greater detail in Section 1.2.3.

1.2 Technical Approach and Current State of the Art

1.2.1 Broadband Metamaterials

Broadband metamaterials are commonly found at RF frequencies utilizing periodic repetition of unit-cells along the wave propagation vector, achieving bandwidth improvements directly analogous to that found in electronic filter design through cascaded filter stages [17]. Practical examples of such cascaded metamaterial transmission lines are multiple layer frequency selective surfaces (FSS) [18-24], electromagnetic band gap (EBG) structures [25-27], and multi-layer absorbers [28].

However, these cascaded designs are not always suitable when weight, thickness, or fabrication constraints (such as the dimensions required at optical wavelengths) are considered. For these reasons a lot of effort has been directed towards making thin profile single layer absorbers. In these designs a single resistive impedance sheet with the appropriate metamaterial geometries can facilitate a thickness much smaller than a wavelength [31]. Early designs successfully demonstrated this phenomenon, albeit at a very narrow frequency band [32, 33]. Rather than relying on tuning known geometries [11, 33], an important and powerful synthesis technique was demonstrated [32] wherein a binary Genetic Algorithm [34-39] was used to generate a pixelated screen. Additional work has extended this technique to single layer absorbers exhibiting multiple absorption bands [40] and, ultimately, broadband single-layer absorbers [41].

Yet, regardless of their application, pixelated metamaterial geometries have two inherent disadvantages. First, diagonally adjacent pixels are often present in optimized designs. Diagonal pixels are problematic because they cannot be fabricated and can cause instabilities in many commercial solvers, requiring further design iterations or an a priori built-in-correction to the design algorithm. Unfortunately, the former approach is not an ideal solution since it requires significant user input, and both methods can undermine the final design's performance. A second concern is that the sharp edges of the pixels become increasingly difficult to manufacture as the feature size decreases, resulting in a greater likelihood for a rounding of edges, causing a degradation and/or a deviation from the expected performance.

In order to resolve these two issues while simultaneously demonstrating a broad bandwidth and low-loss, a new approach for synthesizing metamaterials is introduced in this dissertation. A real valued algorithm, CMA-ES [42], is chosen because of its superior performance among real valued optimizers [43]. CMA-ES is integrated with an algorithm in which two-dimensional (2-D) metasurfaces are synthesized from Bézier surfaces, a computationally efficient method of generating complex shapes from a small sampling of real valued numbers.

To demonstrate the utility of this new metamaterial synthesis method, the problem of improving upon the dielectric wave-plates commonly employed at optical wavelengths [93] is addressed with broad-band, low-loss metasurfaces. In Chapter 2, the theory, metrics for assessing performance, and a study of the performance for known metamaterial geometries is presented [63]. In Chapter 3, the Bézier surface synthesis technique is assessed in terms of algorithm efficiency and final design performance relative to designs generated using the GA approach [64]. The performance of the Bézier surfaces is to not only be superior to the GA synthesized designs; but, also, surpasses performance found in the current literature [65-92].

1.2.2 A Dual-Band Circularly Polarized Antenna Utilizing Dispersion Engineered Metamaterial Radiating Slots

The advantage to realizing useful multiband performance in microstrip patch antennas designs is evident in the literature [95-98]. For the case of dual-band antennas applicable to GPS, GNSS, and WiFi/WiMAX applications, multiple stacked layers are routinely employed [44-54] utilizing varied geometries and approaches [55]. For successful operation, a dual band antenna must radiate a uniform broadside gain pattern at both frequency bands. Such a design task becomes non-trivial if one considers that the upper radiating frequency often utilizes a higher order mode which can greatly distort the radiation pattern and the polarization if not properly addressed. Additionally, designing a feed network that adequately matches both bands can be rather involved; furthermore, the requirement for circularly polarized radiation further complicates the design process. The feeding methods vary for these designs but are generally comprised of aperture-coupled [44, 49-51, 53], multiple feed [46, 48], or wideband microstrip and coaxial probe [47,52] feed networks. The drawbacks of these multiple layered design are fabrication complexity and cost.

Conformal (single layer) designs resolve these problems while attempting to retain small frequency ratios, good axial ratio, and high gain [56-62, 94], in addition to a further fabrication simplification through a reliance on a single probe feed. Yet, while these designs achieve acceptable axial ratios (< 3dB), many rely on higher order modes that result in larger frequency ratios [56-61]. Additionally, the designs exhibit poor gain [57, 60] or do not to specify absolute gain [56, 58, 59, 61, 62], suggesting the performance is rather poor. Lastly, some of these designs rely on very low permittivities, suggesting a possible incompatibility with PCB fabrication techniques, which would limit their utility and increasing the antenna footprint [59, 61].

To address the above issues, a conformal dual-band circularly polarized patch antenna that employs an integrated high Q-factor metamaterial along its radiating slots is presented in Chapter 4. The antenna utilizes a single layer and single coaxial feed, simultaneously exhibiting a small footprint, high gain, and a low axial ratio. The frequency ratio is readily tuned by the metamaterial slots and its reconfigurability is subsequently demonstrated as a function of either capacitive or resistive switching.

1.2.3 Chalcogenides Glass Phase Change Materials Functioning as High Performance Bistable Switches at RF Frequencies

At radio frequencies, there are several common switching technologies utilized to facilitate reconfigurability [99]. Varactors represent the most commonly utilized technology for antenna [100-106], metamaterial, or FSS [107-111] reconfigurability at microwave frequencies. Varactors, which behave as variable capacitors, are attractive due to their low cost and simple integration into RF circuitry. However, varactors are limited in that they exhibit a series resistance, reduced performance above 10GHz due to parasitics. They are also not easily scalable into arrays due to poor tolerances, resulting in varied capacitances across an array [99]. Similarly, PIN diodes or RF switches are essentially varactors that are forward biased and behave as resistive switches. In addition to the drawbacks exhibited by varactors, a PIN diode’s utility is limited by a nontrivial bias current on the order of tens of mA is required, further limiting array scalability due to power constraints. Consequently, examples of antennas [112, 113] and metamaterial FSSs [114] utilizing PIN diodes are less common.

Microelectromechanical systems (MEMS) are an emerging alternative technology is [115]. While the use of packaged MEMS (compatible with PCB fabrication techniques) is most prevalent in reconfigurable microstrip filter and phase shifter designs [116], examples of reconfigurable antennas, FSSs, and metamaterials integrated with packaged MEMS can also be found [117-119, 129, 130-133]. Another common approach is monolithic designs where the MEMS are integrated into the designs using top down manufacturing techniques [120-128]. While MEMS exhibit very high operating frequencies and large on/off ratios, MEMS are limited in utility by their reliance on high bias voltages (~70V-150V) that are difficult to implement and exhibit poor tolerances [99], limiting their utilities in arrays. Furthermore, when compared to semiconductor based switches, MEMS exhibit slower switching speeds (µS) [134].

Among these common switching choices, trade-offs must be made between static power consumption, switch isolation, insertion loss, switching speed, required voltage bias, power handling, cost, and reliability. Thus, any new switching technology that can improve on the currently required trade-offs can have an important impact on RF design.

In Chapter 5, a new RF switching technology is presented. Specifically, a chalcogenide glass (ChG) phase change material (PCM) RF switch technology is presented which improves upon *each* of these aforementioned metrics. To demonstrate its feasibility and performance a multiband reconfigurable FSS integrated with functional ChG PCM switches is also demonstrated in Chapter 5.

1.3 Original Contributions

This dissertation contains several original contributions to the field. They are as follows:

- The introduction of the integration of anisotropic metamaterials with chalcogenide glass phase change material substrates as a means to modulate reflection polarization at long wave infrared wavelengths [63, 138].

- The introduction of an intuitive analytical approach towards realizing broadband dispersion engineered metasurface wave-plates [63, 64, 137].

- The introduction of a new metamaterial geometry that exhibits an intuitive tunability, resulting in microstrip patch antennas with tunable/reconfigurable frequency ratios [136].

- The introduction of a new metamaterial synthesis technique using Bézier surfaces and a real valued optimizer CMA-ES [64, 137]. The algorithm performance is subsequently shown to outperform the commonly used pixelated GA algorithm in terms of computational efficiency and better converged designs.

- The first demonstration and characterization of a ChG PCM (GST) at microwave frequencies, clearing the path for a new high performance RF switch [135].

- The introduction of a quad-state reconfigurable FSS integrated with ChG PCMs that behave as a spectral barcode, applicable to stand-off detection within the X-band communication band.

Chapter 2

Polarization Converting Reconfigurable Metasurfaces at Optical Wavelengths

This chapter introduces alternatives to dielectric wave-plates by using metamaterial based birefringent dielectrics. Analytical solutions and equivalent circuit models are presented for linear and circular polarization splitters, half-wave-plates and quarter-wave-plate metasurfaces. Know metamaterial geometries, the split-ring, the end-loaded dipole, and the meander line, are presented and compared in terms of performance. Reconfigurable polarization is integrated into some of the designs in the form of a substrate that consist of phase change materials. The Stokes parameters are utilized as a metric to assess polarization performance, bandwidth, and scattering efficiency.

2.1 Birefringent Dielectrics

Dielectric wave-plates are comprised of transparent birefringent crystals or polymers. Such anisotropic media are linearly birefringent and change the incident wave polarization into another state such as converting linear polarization into circular polarization. Birefringent media differ from isotropic media in that its D-E constitutive relationships are given by the following vectors

$$\begin{bmatrix} D_x \\ D_y \\ D_z \end{bmatrix} = \begin{bmatrix} \varepsilon_x & 0 & 0 \\ 0 & \varepsilon_y & 0 \\ 0 & 0 & \varepsilon_z \end{bmatrix} \begin{bmatrix} E_x \\ E_y \\ E_z \end{bmatrix}. \tag{2.1}$$

For a birefringent dielectric slab, the ordinary axis has permitivities $\varepsilon_x = \varepsilon_z = \varepsilon_o$ and the extraordinary axis is given as $\varepsilon_y = \varepsilon_e$. For the case of a normally incident plane wave with amplitude *A*, rotated *45°* with respect to the ordinary axis, the electric field is given as

$$\bar{E}(z) = A\frac{\sqrt{2}}{2}(\hat{x} + \hat{y}) \cdot e^{j(\omega t - \hat{k}z)}, \tag{2.2}$$

where

$$\hat{k} = \begin{bmatrix} \omega\sqrt{\mu\varepsilon_o} & 0 & 0 \\ 0 & \omega\sqrt{\mu\varepsilon_e} & 0 \\ 0 & 0 & \omega\sqrt{\mu\varepsilon_o} \end{bmatrix}. \tag{2.3}$$

Dropping the time convention, the solutions for the electric field at a dielectric slab's interfaces (*assuming ideal anti-reflective coatings*) are

$$\bar{E}_{z=0} = A\frac{\sqrt{2}}{2}(\hat{x} + \hat{y})$$

(2.4)

and

$$\bar{E}_{z=l} = A\frac{\sqrt{2}}{2}\left(\hat{x}e^{-jk_x l} + \hat{y}e^{-jk_x l}\right)e^{-jk_z l},$$

(2.5)

where the length of the slab is given as *l*. After simplifying, Equation 2.5 gives

$$\bar{E}_{z=l} = A\frac{\sqrt{2}}{2}\left(\hat{x} + \hat{y}e^{j\left(k_x - k_y\right)l}\right)e^{-jk_x l}.$$

(2.6)

Thus, the relative phase difference between the *x* and *y* components is

$$\phi = \left(k_x - k_y\right)l = \left(n_x - n_y\right)\frac{2\pi l}{\lambda_0}.$$

(2.7)

For a quarter-wave plate, where a linear wave is converted into a circular polarized (CP) wave, the desired phase difference is

$$\phi = \frac{\pi}{2} = (n_x - n_y)\frac{2\pi l}{\lambda_0},$$

(2.8)

resulting in the following relationship

$$(n_x - n_y)l = \frac{\lambda_0}{4}.$$

(2.9)

Similarly, for a half wave plate, where a linear wave is rotated by 90°, the phase relationship is

$$(n_x - n_y)l = \frac{\lambda_0}{2}.$$

(2.10)

2.1.1 Dielectric Quarter-Wave Plate Represented by the Stokes Parameters

2.1.1.1 Stokes Parameters

In order to convey the degree of circular polarization transmitted by the quarter-wave plate, the Stokes vector is used. The Stokes vector completely describes the polarization of a wave in terms of amplitude and the degree of polarization using four parameters

$$S = \begin{bmatrix} I \\ Q \\ U \\ V \end{bmatrix}.$$

(2.11)

The Stokes parameter I corresponds to the total intensity of the reflected or transmitted wave. The Stokes parameter $\pm Q$ corresponds to a horizontally or vertically oriented linear polarization, respectively. Similarly, the $\pm U$ Stokes parameter corresponds to a horizontal or a vertical linear polarization, each of which have been rotated 45° degrees counter-clockwise. Lastly, the $\pm V$ Stokes parameter corresponds to right hand or left hand circular polarization, respectively. These parameters and a corresponding graphical representation of the polarization vector are depicted in Figure 2.1.

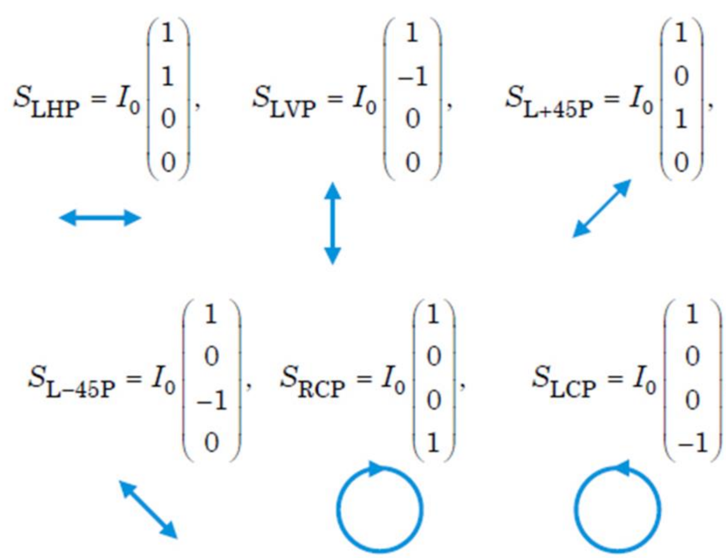

Figure 2.1. Stokes vectors with corresponding parameters and polarization depictions.

To calculate the Stokes parameters for a scattered wave in Cartesian coordinates, the following relationships to the normalized complex electric fields are used

$$I = |E_x|^2 + |E_y|^2, \tag{2.12}$$

$$Q = |E_x|^2 - |E_y|^2, \tag{2.13}$$

$$U = 2Re(E_x E_y^*), \tag{2.14}$$

$$V = -2Im(E_x E_y^*). \tag{2.15}$$

2.1.1.2 Quarter-Wave Plate Using a Birefringent Crystal.

As an example, a birefringent crystal, calcium carbonate ($n_o \approx 1.66$ and $n_e \approx 1.5$), is used as the medium for a quarter-wave plate centered at $\lambda = 1.55\ \mu m$. The results, utilizing the analytical expression given in Equation 2.9, are summarized in Figure 2.2. The plots are of the first four orders of a birefringent quarter-wave plate. The orders correspond to the initial length that results in the quarter-wave condition (i.e. zeroth order) followed by higher orders which refer to additional length increases corresponding to 2π phase permutations, respectively. For these solutions the *I*-parameter equals unity, corresponding to complete transmission given by our assumed loss-less and reflection-less crystal. The *V*-parameter equals negative one at our operating wavelength of 1.55 μm, corresponding to a purely left hand circular polarized transmitted wave. The zero order quarter-wave plate, with our assumed indices of refraction, results in a length of l = 2.422 μm whereas subsequent orders add $9.688\ \mu m$ to the length for each 2π permutation. The transmitting quarter-wave plate can be configured as a reflecting quarter-wave plate by reducing the length by a factor of 2 and backing the structure with a highly reflective metal surface, yielding the same response in terms of reflection rather than transmission. This response shows that the bandwidth of the quarter-wave plate is inversely proportional to the order of the structure. However, this idealized response neglects several key factors, namely the feasibility of the aforementioned requirement for an ideal anti-reflective coating in addition to the omission of loss and dispersion which will further limit efficiency and bandwidth. This is especially true in the context of atomic resonances that can be described by the Drude-Lorentz dispersion model. They can render a specific material unusable at certain wavelengths due to increased absorption. Lastly, the length of the crystal does not take into account any mechanical requirements of the structure. Since the prescribed thickness is a direct function of the magnitude of birefringence that a material exhibits, it cannot be assumed that a zeroth-order wave plate or a highly birefringent crystal like calcium carbonate is practical in all cases. Nevertheless, the results serve as a frame of reference for the comparison to metasurface performance.

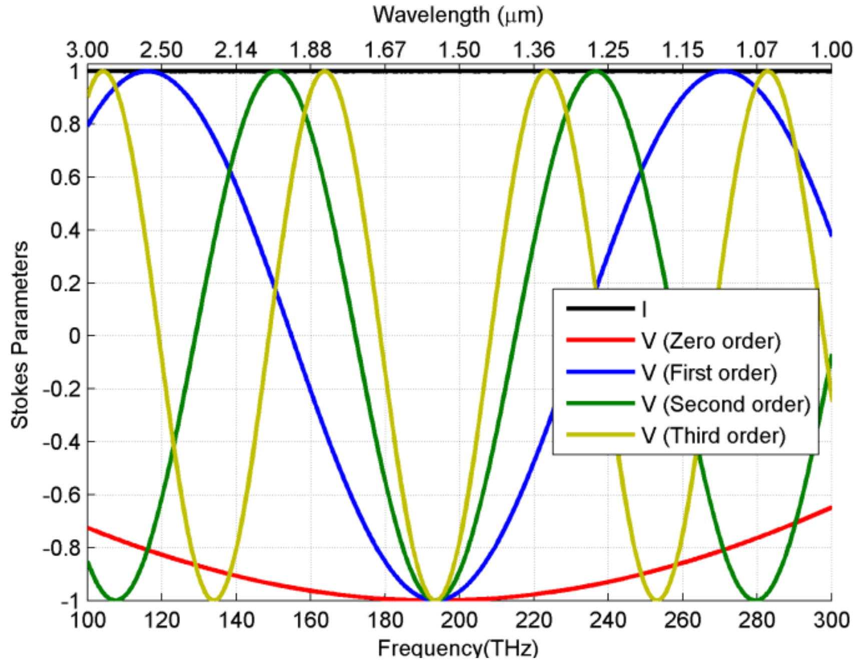

Figure 2.2. Stokes V-parameter for zero through third order reflection-less quarter-wave plate responses.

2.2 Anisotropic Metasurfaces

In this section, it will be shown that an anisotropic metasurface, consisting of a 2-D infinitely periodic array of sub-wavelength metallic resonators, can behave as a polarization splitter and can subsequently be configured as a polarization splitter or, through the addition of a ground plane, as either a quarter-wave or a half-wave plate. To analytically demonstrate the polarization conversion of the anisotropic metamaterial, a normally incident plane wave,

$$\bar{E}_{inc} = E_0(\cos\varphi\,\hat{x} + \sin\varphi\,\hat{y}) \cdot e^{j(\omega t - \hat{k}z)},$$

(2.11)

is assumed to be horizontally polarized (i.e. $\varphi=0$) and in phase at the interface of the metasurface such that in vector form,

$$\bar{E}_{inc} = \begin{bmatrix} 1 \\ 0 \end{bmatrix}. \tag{2.16}$$

In order to simplify successive derivations, the amplitude has been normalized while the time and frequency dependence has been suppressed.

Furthermore, it will be shown that a plane wave normally incident to the surface of an ideal planar metamaterial, the interaction, or more specifically the linear, lossless scattering of polarized light, can be described in a manner similar to the Jones matrix calculus [168], in which the amplitudes of the reflected wave in terms of co-polarization and cross-polarization for a two port system are contained in a 2 by 2 matrix.

2.2.1 Anisotropic Impedances

Beginning with an anisotropic impedance surface,

$$\hat{Z} = \begin{bmatrix} Z_x & 0 \\ 0 & Z_y \end{bmatrix}, \tag{2.17}$$

the reflection matrix for a plane wave traveling in free space is,

$$\hat{\Gamma} = \begin{bmatrix} \Gamma_x & 0 \\ 0 & \Gamma_y \end{bmatrix}.$$

(2.18)

The anisotropic reflection coefficient in free space is calculated in the usual manner:

$$\hat{\Gamma} = \frac{\hat{Z} - \eta}{\hat{Z} + \eta}.$$

(2.19)

Rotating the reflection matrix azimuthally, we transform the reflection matrix using the rotation matrix,

$$R(\varphi) = \begin{bmatrix} \cos\varphi & -\sin\varphi \\ \sin\varphi & \cos\varphi \end{bmatrix},$$

(2.20)

as follows:

$$\hat{\Gamma}(\varphi) = R(\varphi) \cdot \hat{\Gamma} \cdot R(-\varphi),$$

(2.21)

which, when rotated by *45°*, gives:

$$\hat{\Gamma}_{\varphi=\frac{\pi}{4}} = \frac{1}{2}\begin{bmatrix} \Gamma_x + \Gamma_y & \Gamma_x - \Gamma_y \\ \Gamma_x - \Gamma_y & \Gamma_x + \Gamma_y \end{bmatrix}.$$

(2.22)

2.2.2 Linear Wave Decomposition

Referencing Equation 2.22, a linearly polarized incident wave can be decomposed into two equal amplitude *U*-polarized waves of opposite handedness,

$$\bar{E}_{inc} = \begin{bmatrix} 1 \\ 0 \end{bmatrix} = \frac{1}{2}\begin{bmatrix} 1 \\ -1 \end{bmatrix} + \frac{1}{2}\begin{bmatrix} 1 \\ 1 \end{bmatrix}. \tag{2.23}$$

Alternatively, the incident wave can also be decomposed into two equal amplitude *V* polarized waves of opposite handedness,

$$\bar{E}_{inc} = \begin{bmatrix} 1 \\ 0 \end{bmatrix} = \frac{1}{2}\begin{bmatrix} 1 \\ j \end{bmatrix} + \frac{1}{2}\begin{bmatrix} 1 \\ -j \end{bmatrix}. \tag{2.24}$$

We can use these results and treat them as the desired scattering responses for two types of anisotropic metasurface polarization splitters. Specifically, the first design will scatter a +*Q*-incident wave into a +*U*-polarized reflected and a –*U*-polarized transmitted wave. The second design will scatter a +*Q*-incident wave into a +*V*-polarized reflected and a –*V*-polarized transmitted wave (see Figure 1.3).

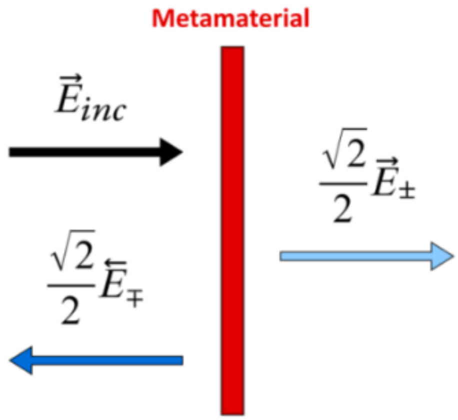

Fig. 2.3. Scattered field handedness, amplitude, and propagation direction for an anisotropic metasurface illuminated by a linearly polarized incident field.

2.2.3 Polarization Splitters

2.2.3.1 Linearly Polarized Splitter

Utilizing Equation 2.22, the desired response for the reflected wave for a linearly polarized splitter can be expressed as

$$\bar{E}_{ref} = \frac{1}{2}\begin{bmatrix} \Gamma_x + \Gamma_y & \Gamma_x - \Gamma_y \\ \Gamma_x - \Gamma_y & \Gamma_x + \Gamma_y \end{bmatrix}\begin{bmatrix} 1 \\ 0 \end{bmatrix} = \frac{1}{2}\begin{bmatrix} -1 \\ 1 \end{bmatrix}. \tag{2.25}$$

A solution for the reflection coefficients yields

$$\Gamma_x = 0 \text{ and } \Gamma_y = -1.$$

(2.26)

Referencing the equivalent circuit depicted in Figure 2.4, these reflection coefficients result from a shunt short circuit and a shunt open circuit, respectively.

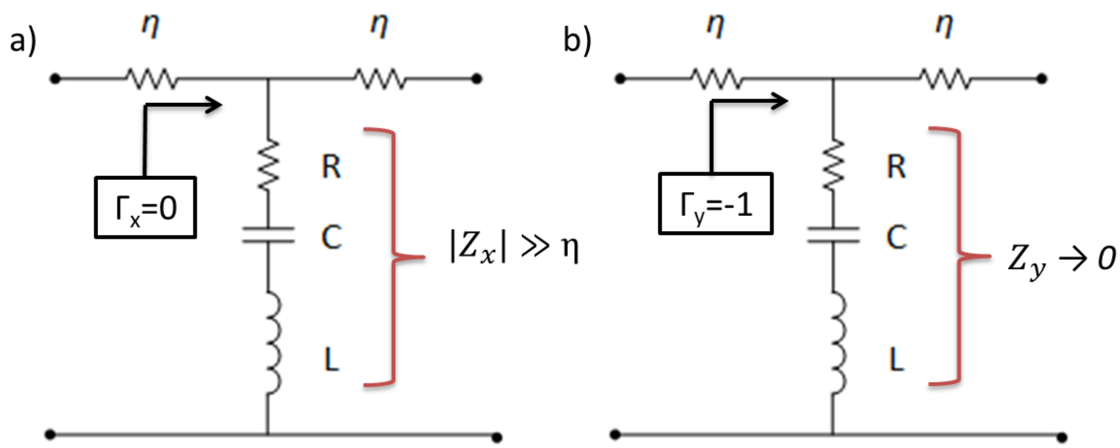

Figure 2.4. Equivalent circuit model for a linearly polarized metasurface splitter for (a) horizontal and (b) vertical polarizations, respectively.

2.2.3.2 Circularly Polarized Splitter

Next, for the case of a circularly polarized splitter the desired response for the reflected wave can be expressed as:

$$\bar{E}_{ref} = \frac{1}{2}\begin{bmatrix} \Gamma_x + \Gamma_y & \Gamma_x - \Gamma_y \\ \Gamma_x - \Gamma_y & \Gamma_x + \Gamma_y \end{bmatrix}\begin{bmatrix} 1 \\ 0 \end{bmatrix} = \frac{1}{2}\begin{bmatrix} -1 \\ j \end{bmatrix}.$$

(2.27)

A physical solution for the reflection coefficients yields

$$\Gamma_x = \frac{\sqrt{2}}{2} e^{j\frac{3\pi}{4}} \text{ and } \Gamma_y = \frac{\sqrt{2}}{2} e^{-j\frac{3\pi}{4}},$$

(2.28)

where it is emphasized that

$$\Gamma_x = \Gamma_y^{\,*}.$$

(2.29)

As depicted by the equivalent circuit in Figure 2.5, these reflection coefficients result from a shunt positive and negative reactance, respectively. The magnitudes of each reactance can be approximated as equal to $\eta/2$.

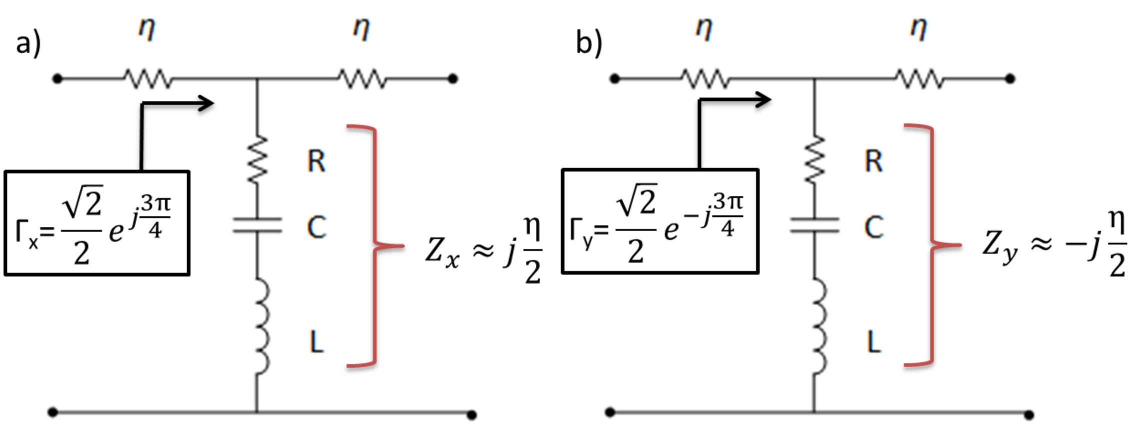

Figure 2.5. Equivalent circuit model for a circularly polarized metasurface splitter for (a) horizontal and (b) vertical polarizations respectively.

2.3.4 Analytical Solutions for Wave-plates

2.2.4.1 Half-Wave Plate

If the transmitted wave is reflected backwards by the introduction of a conductive sheet with an electrical standoff length of $l = \lambda/4$, then the reflection coefficients become $\Gamma=\pm 1$. The resultant equivalent circuit is shown in Figure 2.6. The reflection coefficients are now

$$\Gamma_x = 1 \text{ and } \Gamma_y = -1. \tag{2.30}$$

Utilizing Equation 1.22, the response for the reflected wave for a half-wave plate can be expressed as

$$\bar{E}_{ref} = \begin{bmatrix} 0 & 1 \\ 1 & 0 \end{bmatrix} \begin{bmatrix} 1 \\ 0 \end{bmatrix} = \begin{bmatrix} 0 \\ 1 \end{bmatrix}. \tag{2.31}$$

The polarization response of this half-wave plate as a function of azimuthal rotation (i.e. using Equation 2.21) is shown in Figure 2.7.

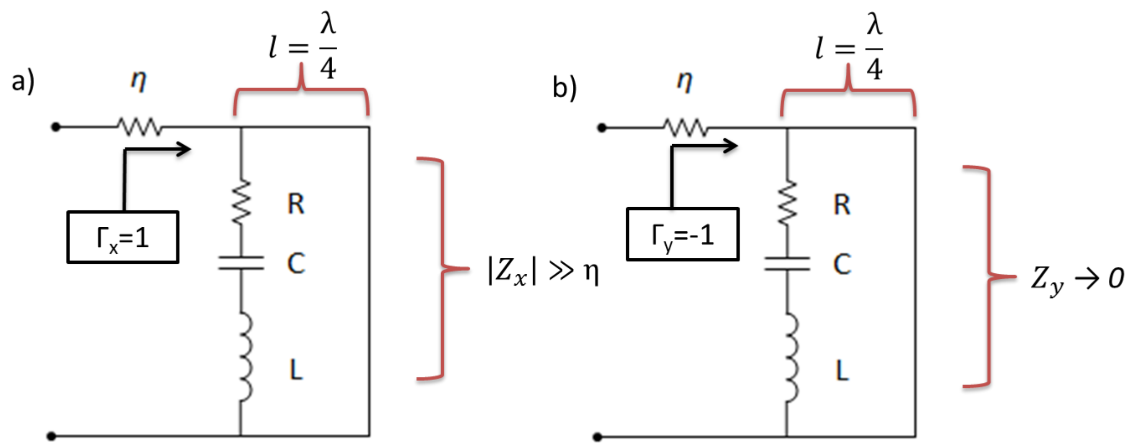

Figure 2.6. Equivalent circuit model for a half-wave plate metasurface for (a) horizontal and (b) vertical polarizations, respectively.

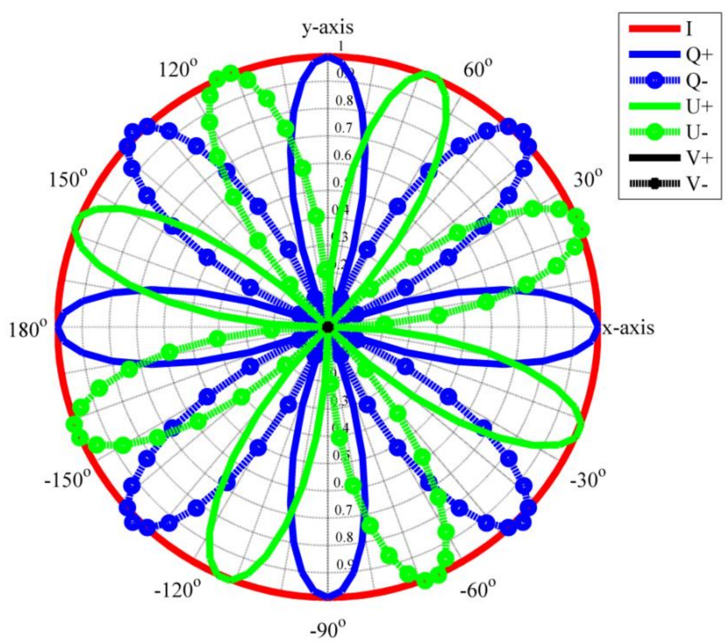

Figure 2.7. Stokes parameters for a half-wave plate metasurface as a function of azimuthal rotation.

2.2.4.2 Quarter-Wave Plate

Similarly, for a circularly polarized splitter the transmitted wave is reflected backwards by the introduction of a conductive sheet with an electrical standoff length of $l = \lambda/4$. The resulting reflection coefficients are

$$\Gamma_x = e^{j\frac{3\pi}{4}} \text{ and } \Gamma_y = e^{-j\frac{3\pi}{4}}. \tag{2.32}$$

The resultant equivalent circuit is shown in Figure 2.8. Utilizing Equation 2.22 again, the response for the reflected wave for a quarter-wave plate can be expressed as:

$$\bar{E}_{ref} = \frac{\sqrt{2}}{2}\begin{bmatrix} -1 & j \\ j & -1 \end{bmatrix}\begin{bmatrix} 1 \\ 0 \end{bmatrix} = \frac{\sqrt{2}}{2}\begin{bmatrix} -1 \\ j \end{bmatrix}. \tag{2.33}$$

The polarization response of this quarter-wave plate as a function of azimuthal rotation is depicted in Figure 2.9.

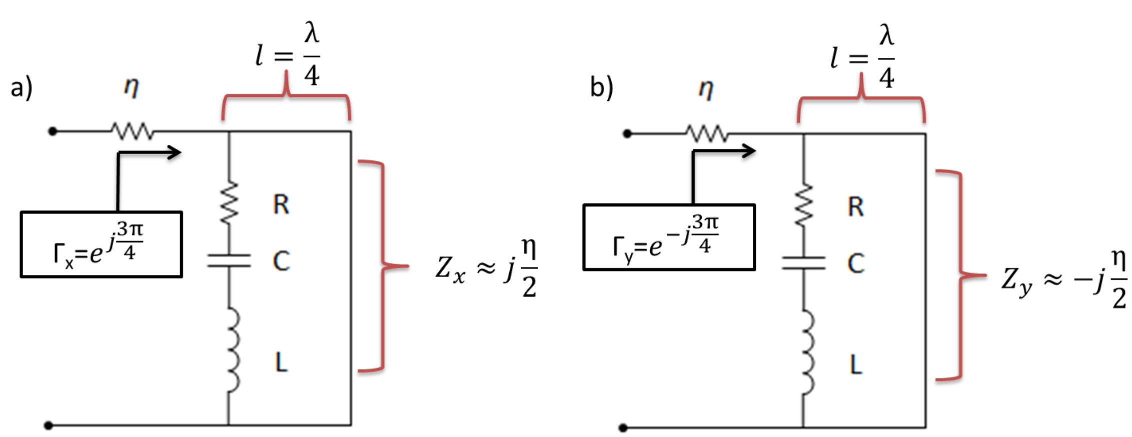

Figure 2.8. Equivalent circuit model for a quarter-wave plate metasurface for (a) horizontal and (b) vertical polarizations, respectively.

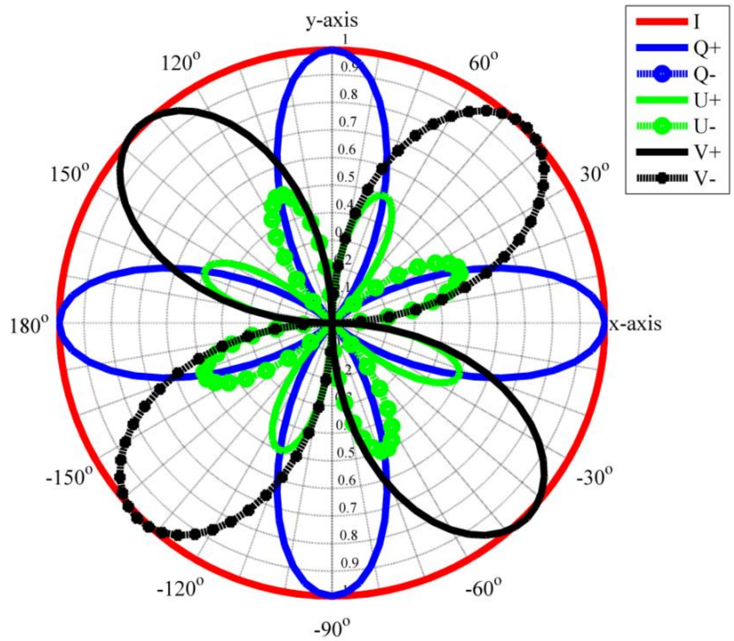

Figure 2.9. The Stokes parameters for a quarter-wave plate metasurface as a function of azimuthal rotation.

2.3.5 Broadband Quarter-Wave-plates

2.3.5.1 Short-Wavelength Infrared Broadband Quarter-Wave Plate

Through dispersion engineering, the concept of broadband metamaterial wave-plates can be realized. By engineering the anisotropic Lorentzian resonances for a wave plate metasurface, we can mitigate losses and maximize bandwidth over a wide field of view. To demonstrate this concept, designs operating within the short-wavelength infrared are simulated. Each design consists of a 2-D-infinitely periodic array of an anisotropic metasurface geometry. The first design is a dipole and the second one is a split-ring. Both structures exhibit anisotropic Lorenzian resonances that are staggered in terms of frequency. For both designs, vertically polarized light excites the first resonance at the lower frequency whereas the upper frequency bounds are determined by a resonance that occurs due to horizontally polarized light.

The first anisotropic metasurface (Figure 2.10 (a)) is a 2-D infinitely periodic array that consists of capacitively end-loaded dipole elements. The unit-cell is 480 nm x 480 nm, and the dipole is comprised of 75 nm thick Au supported by a 75 nm polyimide substrate and backed by a 200 nm Au ground plane. The lower resonance, ω_1, caused by the decomposition of an incident linear wave parallel to the dipole axis falls into the realm of metamaterial (*i.e.* sub-wavelength) behavior due to the size reduction caused by the capacitive end-loading of adjacent unit-cells. However, the orthogonal resonance, ω_2, does not occur at a sufficiently long wavelength because it is attributed to the formation of a dependent grating which is in turn highly angularly dependent. Consequently, a very broadband CP design is achieved at normal incidence but performance degrades rapidly for increasing oblique angles, thereby limiting the utility of the design.

The second anisotropic metasurface (Figure 2.10 (b)) is a 2-D infinitely periodic array consisting of split-ring elements. The unit-cell is 380 nm x 380 nm and the SR is comprised of 75 nm thick Au supported by a 50 nm polyimide substrate and backed by a 200 nm Au ground plane. The lower resonance, ω_1, is caused by the decomposition of an incident linear wave perpendicular to the SR gap. The upper orthogonal resonance is caused by the decomposition of an incident linear wave parallel to the SR gap. Both resonances fall within the realm of metamaterial behavior due to the retention of a sufficiently sub-wavelength geometry at both frequencies. This directly results in a broadband CP reflector with a wide field of view (FOV). By properly engineering the dispersion of the anisotropic, frequency-offset resonances we can retain a very wide field of view while also exhibiting low loss and a broad-bandwidth for polarization conversion. For easier comparison with other metrics of assessing the degree of circular polarization found elsewhere, the performance of the split-ring design of Figure 2.10 (b) is represented in Figure 2.11 in the full Stokes parameters, the Stokes parameters as a function of azimuthal rotation within its band of operation, axial ratio and finally polarization conversion ratio.

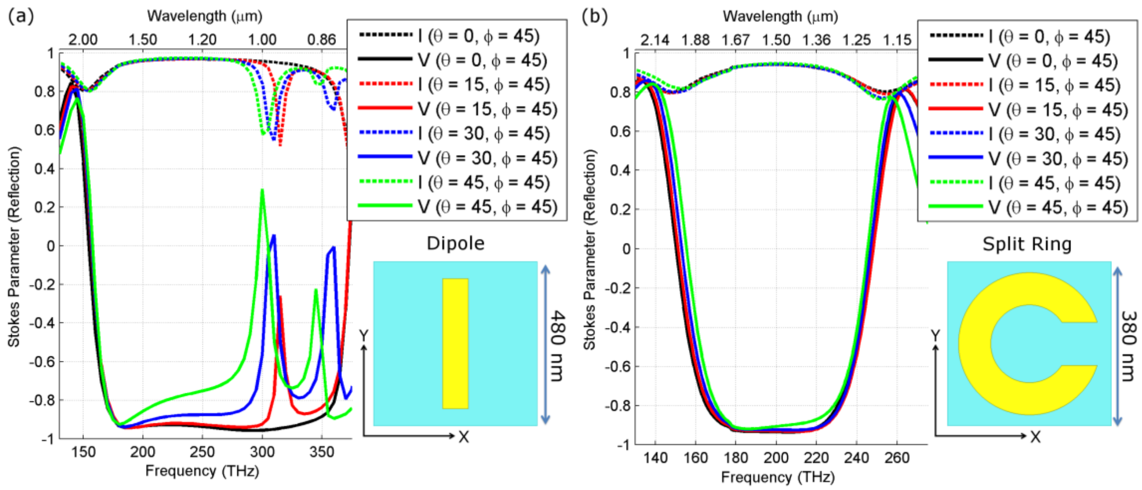

Figure 2.10. Dispersive Stokes *I* and *V* parameters as a function of angle of incidence for (a) a dipole and (b) a split-ring metasurface (*note the difference in x-axis scale between the two designs).

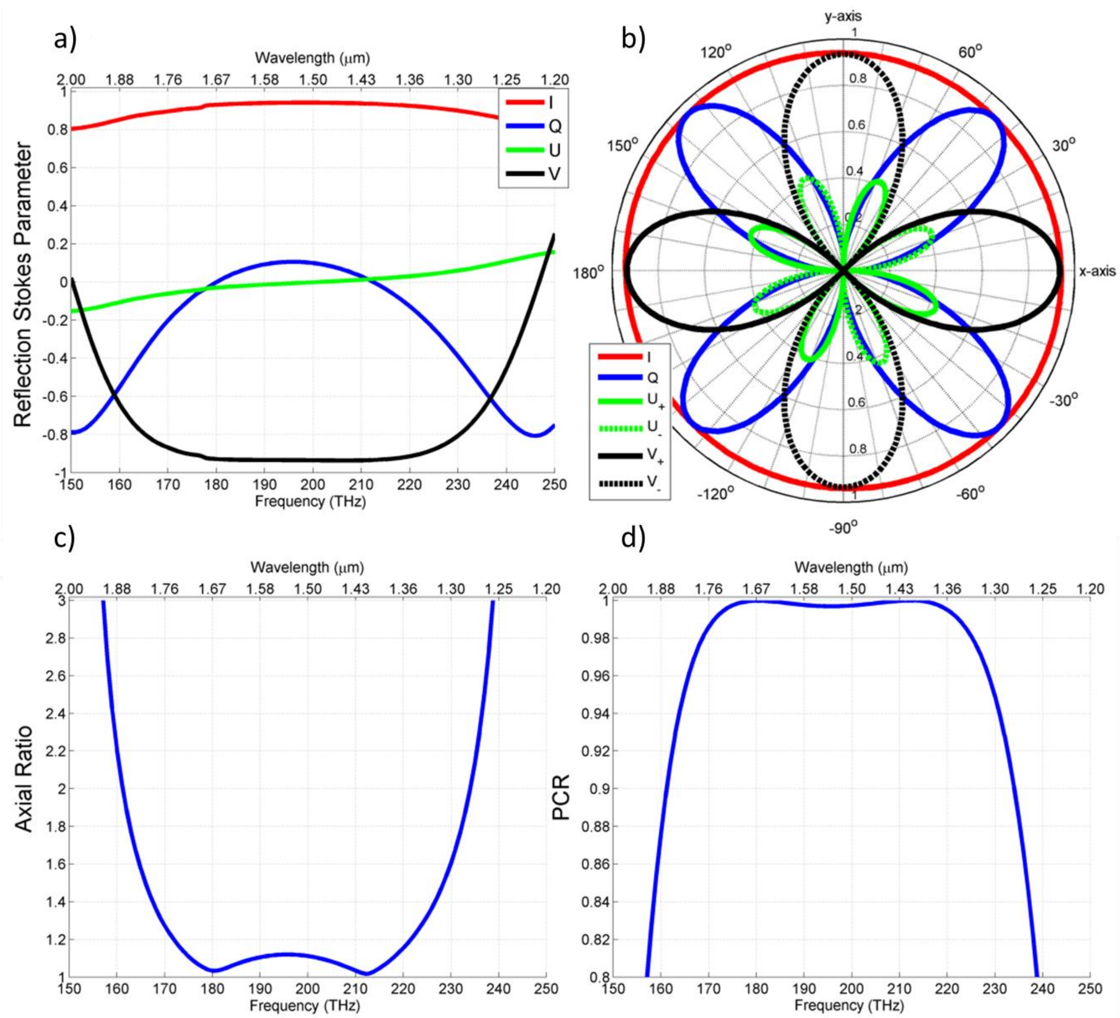

Figure 2.11. (a) Stokes parameters, (b) Stokes parameters as a function of azimuthal rotation, (c) axial ratio, and (d) polarization conversion ratio for the split-ring design from Figure 2.10(b).

2.3.5.2 Long-Wavelength Infrared Reconfigurable Quarter-Wave Plate

The utility of the circularly polarizing metasurface can be increased if reconfigurability is introduced; because, polarization sensing can offer a lower signal to noise ratio than amplitude modulation [63]. Reconfigurability is facilitated by incorporating a phase change material (PCM) into the substrate. In the amorphous state, the substrate will be insulating and the metasurface will function as a quarter-wave plate metasurface. When the PCM is converted into the crystalline state, the substrate becomes conductive, shorting out the metasurface layer. As a result, the structure behaves as a metallic mirror. The Stokes parameters of a reconfigurable quarter-wave metasurface are plotted as a function of azimuthal rotation in Figure 2.13 for both the amorphous and the crystalline PCM phase states, respectively.

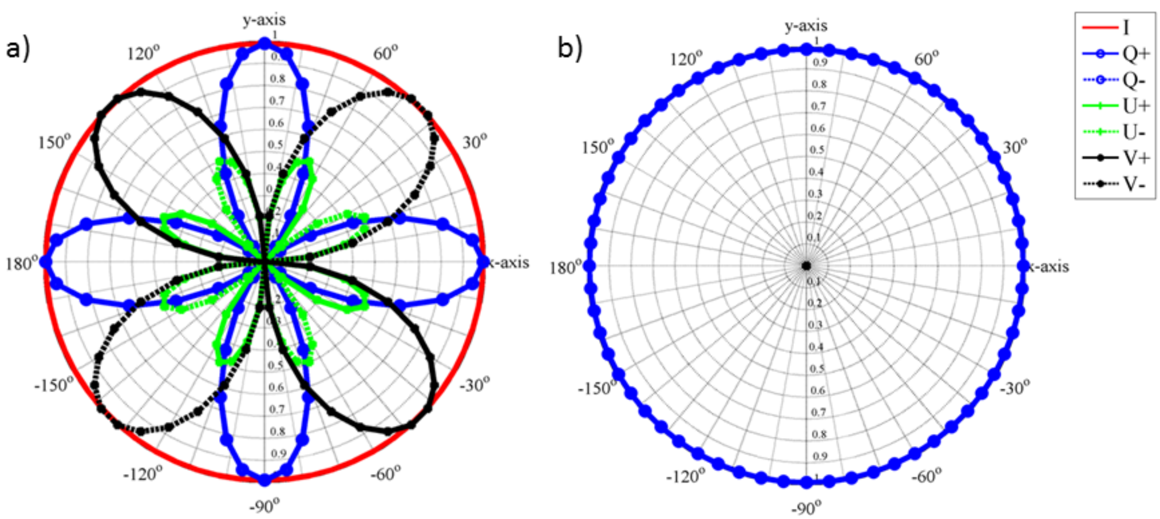

Figure 2.12. Ideal Stokes parameters for a quarter-wave metasurface as a function of azimuthal rotation given a GST substrate in the (a) amorphous or (b) crystalline state.

Three known metamaterial geometries, the end-loaded dipole, the meander-line and the split-ring are utilized and there performances are compared in this reconfigurable configuration. These three examples are designed for the atmospheric window within the long-wave infrared band (8 µm to 12 µm). Each design incorporates a $Ge_2Sb_2Te_5$ (GST) chalcogenide (ChG) PCM substrate and functions as a circular polarizer when the GST is in the amorphous state. In the crystalline state, the substrate becomes lossy, resulting in a metallic, mirror-like reflection with no polarization conversion. The measured values utilized for GST at $\lambda=10\mu m$ are $n = 4.2$, $k = 0.01$ in the amorphous state and $n = 8$, $k = 4.8$ in the crystalline state [63]. As with the near IR designs, full-wave simulations consider all losses using material parameters measured by ellipsometry.

The first geometry is a 2-D infinitely periodic metasurface that consists of end-loaded dipole elements. The unit-cell is 700 nm x 700 nm and the dipole is comprised of 150 nm thick Au, supported by a 430 nm GST substrate, and backed by a 150 nm Au ground plane. The lower resonance, ω_1, is caused by the decomposition of an incident linear wave parallel to the dipole axis. The orthogonal resonance, ω_2, is attributed to the higher Q end load resonance. Since the structure is sufficiently sub-wavelength angular performance is good (Figure 2.13(a)), but the asymmetrical Q-factors exhibit markedly different dispersion properties and result in a limited region of high CP.

The second geometry is a 2-D infinitely periodic metasurface that consists of meander line elements. The unit-cell is 900 nm x 1800 nm and the meander line is comprised of 150 nm thick Au supported by a 400 nm GST substrate and backed by a

150 nm Au ground plane. While exhibiting a broad bandwidth and similar Q-factors for the lower and upper resonances (Figure 2.13(b)), the large unit-cell length results in a deterioration of angular performance, as indicated by the emergence of an in-band resonance at larger oblique angles.

The third geometry is the familiar SR design with appropriate geometry scaling. The unit-cell is 975 nm x 975 nm and the SR is comprised of 150 nm thick Au, supported by a 465 nm GST substrate, and backed by a 150 nm Au ground plane. Since the structure is sufficiently sub-wavelength and exhibits highly symmetric Q factors, broad bandwidth and good angular performance are exhibited (Figure 2.13(c)). This design is used to demonstrate in Figure 2.14(d) that when the GST substrate phase is changed to the crystalline state the structure no longer behaves as a broadband birefringent surface but rather as a metallic mirror.

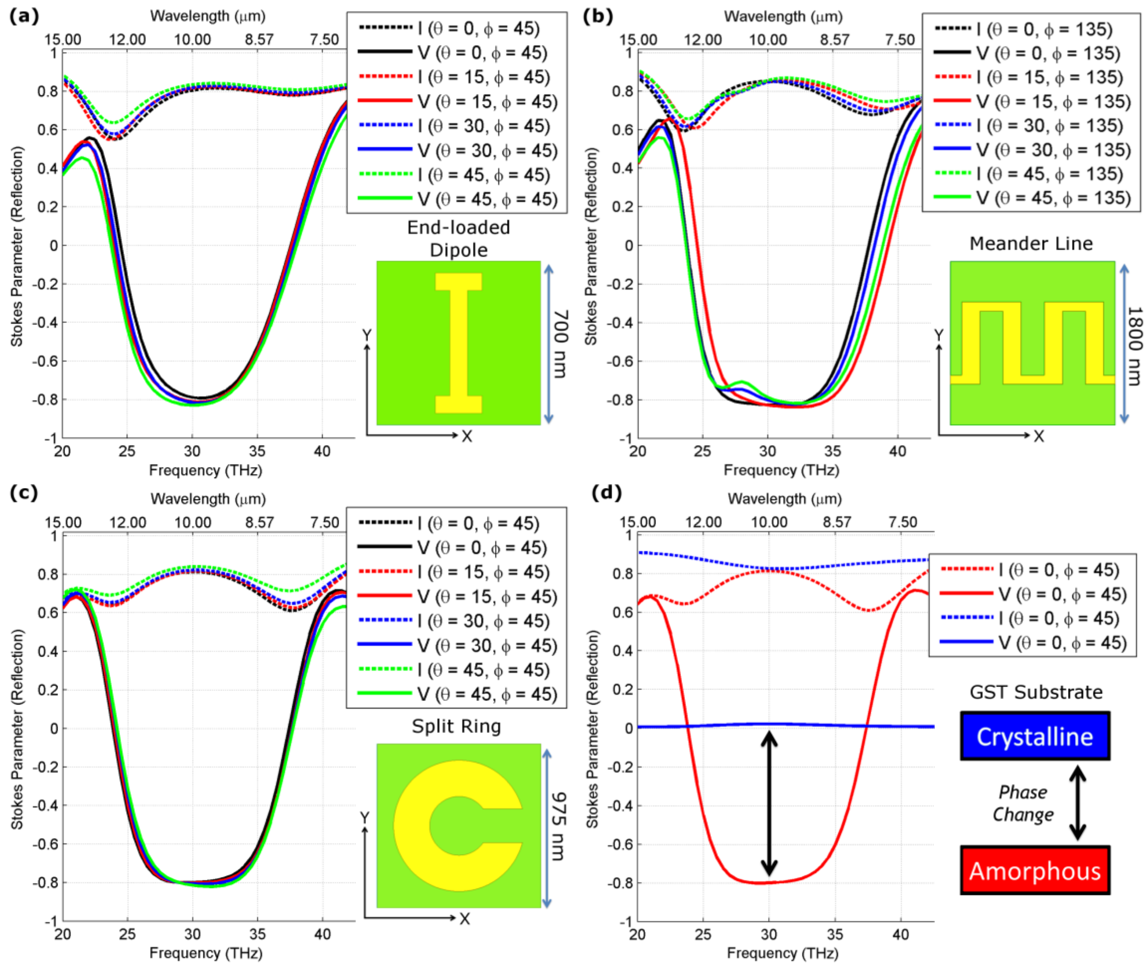

Figure 2.13. Dispersive Stokes *I* and *V* parameters as a function of angle of incidence for (a) an end-loaded dipole, (b) a meander line, and (c) a split-ring. (d) Depicts the Stokes *I* and *V* parameters as a function of the GST substrate phase state.

Chapter 3

Optimized Bézier Metasurfaces Wave-plates

The previous chapter has shown that known anisotropic metamaterial geometries can be used as broadband metasurface wave-plates when the dispersion is properly tuned. Yet, the question remains whether these known designs represent the best realizable performance or if better performance is attainable through the synthesis of new geometries. In this chapter, a new technique for optimizing 2-D periodic anisotropic metasurfaces is presented that perform significantly better than commonly used geometries found in the recent literature [65-92]. Specifically, the Bézier surface [139] is introduced as an effective design tool to obtain very broadband metasurface-enabled IR quarter-wave and half-wave-plates. To demonstrate the effectiveness of this Bézier surface synthesis technique, a real valued optimizer, CMA-ES [42], is used to synthesize the metasurfaces. The computational efficiency and performance of the optimized Bézier surfaces is compared to an existing and well known optimization technique for pixelated structures synthesized via a binary GA [34-39]. When compared to the GA optimized pixelated structures, the synthesis of Bézier surfaces using CMA-ES is shown to not only provide better results but also to generate them with an order of magnitude reduction in computation time. In order to further demonstrate the advantages of the proposed Bézier metasurface synthesis technique, a broadband reconfigurable quarter-wave plate is designed for the 8 μm to 12 μm band and subsequently shown to exhibit improved performance when compared to SR design from the previous chapter. Additionally, a multi-octave IR linear polarization splitter and quarter-wave and half-wave plate Bézier metasurface designs are presented with bandwidths surpassing the MWIR.

3.1 The Bézier Surface

Historically, the origin of the Bézier curve and Bézier surface can be traced to Bernstein's proof of the Weierstrass approximation theorem. The Weierstrass approximation theorem states that polynomials can uniformly approximate any function which is continuous over a given interval. Bernstein's proof of the Weierstrass theorem employs only basic algebraic functions; thus, its form is conducive to rapid computation. The Bernstein polynomial with any continuous function *f(t)* is given as

$$P_n(x) = \sum_{k=0}^{n} f(k/n)\, B_k^n(x), \tag{3.1}$$

with the Bernstein basis defined as

$$B_k^n(x) = \binom{n}{k} x^k (1-x)^{(n-k)}, k = 0, \dots, n. \tag{3.2}$$

In the early 1960s, De Casteljau and Bézier began investigating mathematical tools applicable to automotive body design which would provide intuitive and accurate methods to create and subsequently convey complex shapes which were not easily defined by simple geometric parameters. Their work lead to an adaptation of the Bernstein polynomial to what is now referred to as the Bézier curve

$$P_n(x) = \sum_{k=0}^{n} C_k \, B_k^n(x) \tag{3.3}$$

where C_k represents the amplitude and position for the control points to be manipulated. An example of a Bézier curve is shown in Figure 3.1. Only five (*i.e.*, $n = 5$) control points are used to define the complex curve.

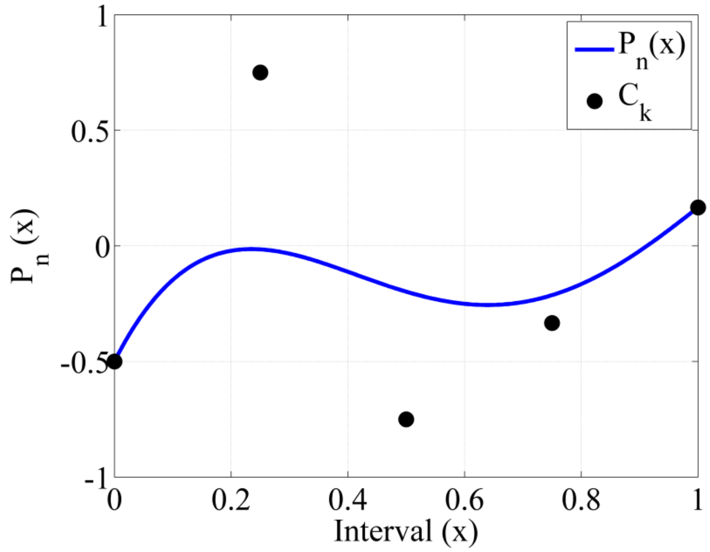

Figure 3.1. A Bézier curve (blue) plotted as a function of x with n = 5 control points (black).

This approach can now be extended to three dimensions via the introduction of a Bézier surface which is simply represented as

$$P_{n,m}(x,y) = \sum_{i=0}^{n}\sum_{j=0}^{n} C_{i,j}\, B_i^n(x) B_j^m(y)$$

(3.4)

The control points are now defined as amplitudes contained within a matrix of arbitrary size (*m x n*)

$$C_{i,j} = \begin{pmatrix} C_{11} & \cdots & C_{1m} \\ \vdots & \ddots & \vdots \\ C_{n1} & \cdots & C_{nm} \end{pmatrix}$$

(3.5)

An example of a Bézier surface is shown in Figure 3.2, where a five by five matrix (*i.e.*, $m = 5$, $n = 5$) of control points is used to define the complex surface. Figure 3.3 depicts the positive values of the Bézier surface projected onto the $z = 0$ plane. This projection illustrates the approach used to synthesize metasurface geometries in the following section.

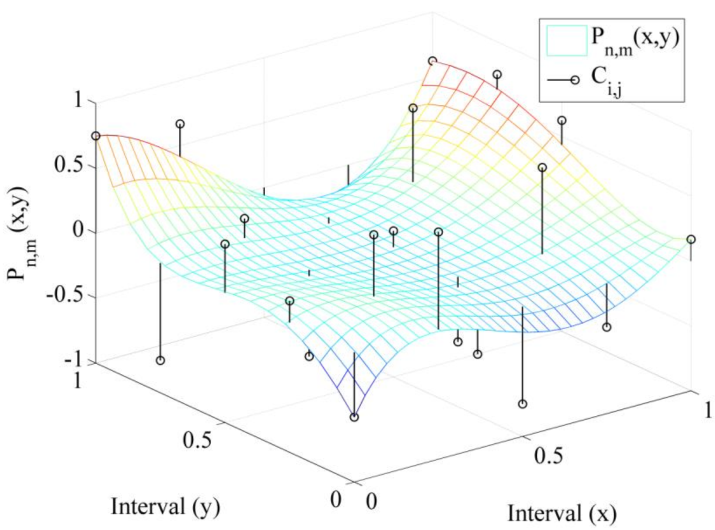

Figure 3.2. Plot of a $m=5$, $n=5$ Bézier surface (color) with control points shown (black).

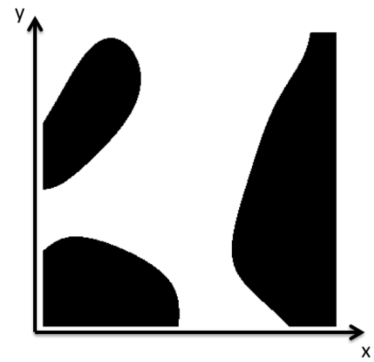

Figure 3.3. Plot of the positive values of the Bézier surface in Figure 3.2 projected onto the $z = 0$ axis.

3.2 Bézier Metasurface Synthesis

It can be reasonably inferred that fabricating structures synthesized via Bézier surfaces will have an inherent advantage over the conventionally used pixelated structures when considering relative geometrical complexity, especially for optical metasurface-enabled devices. This is attributed to the greater ease in the manufacturing of the Bézier surface's continuous contours versus the potential difficulty in realizing the finer features of a pixelated structure, especially in the case of numerous diagonally adjacent pixels. In addition to fabrication complexity of generated designs, another concern when optimizing structures is the overall time it takes to complete the required simulations. Global optimizers generally take thousands of evaluations to arrive at good results. Therefore, considering that full-wave electromagnetic solvers are notoriously slow, any demonstrable increase in the speed of an optimization is highly desirable. In order to assess the computational efficiency of the Bézier surface optimization, a GA is used as a reference optimizer. The binary GA has been widely used to generate pixelated metasurfaces at radio frequencies (RF) and optical wavelengths for several decades [32-39]. While the GA is a binary algorithm, the Bézier surface is optimized by a real valued algorithm CMA-ES which has been shown to be very efficient and reliable at solving real valued problems [43]. CMA-ES is linked to the Bézier surface through the optimization of a 10 by 5 matrix of control points (see Equation 3.5) with the values of individual control points ranging from -1 to 1. For the algorithms' comparison, the initial populations for both algorithms are generated by the same 20 seeds.

The use of the same seeds allows for a direct comparison between the two algorithms by ensuring that they have the same initial random populations, whereas the use of multiple seeds helps in assessing the overall algorithm performance. The progress and overall performance of the algorithms are assessed by their ability to minimize the error from ideal performance as a function of the number of completed simulations. The deviation from optimal performance is defined by a fitness function which for this study is defined as

$$fitness = \sum_{frequency} ((1 - I)^2 + Q^2 + U^2 + (1 - |V|)^2) \tag{3.6}$$

where the Stokes parameters are utilized to assess the degree of circular polarization across the 8 μm to 12 μm band.

3.2.1 Performance Comparisons Between Optimized Pixelated and Bézier Surfaces

Figure 3.4(a) depicts the performance of each optimization conducted for 20 seeds. For both algorithms, the mean fitness of all seeds, the median fitness of all seeds, and the seed with the best fitness are plotted in terms of fitness value versus the number of function evaluations. Figure 3.4(b) and Figure 3.4(c) depict the best seed's performance for the GA (pixelated surface) and CMA-ES (Bézier surface) respectively. It is clear that the Bézier surface optimized via CMA-ES not only provides better final results than the GA optimized pixelated surfaces; but, it also achieves superior solutions with more than an order of magnitude reduction in the number of required function evaluations.

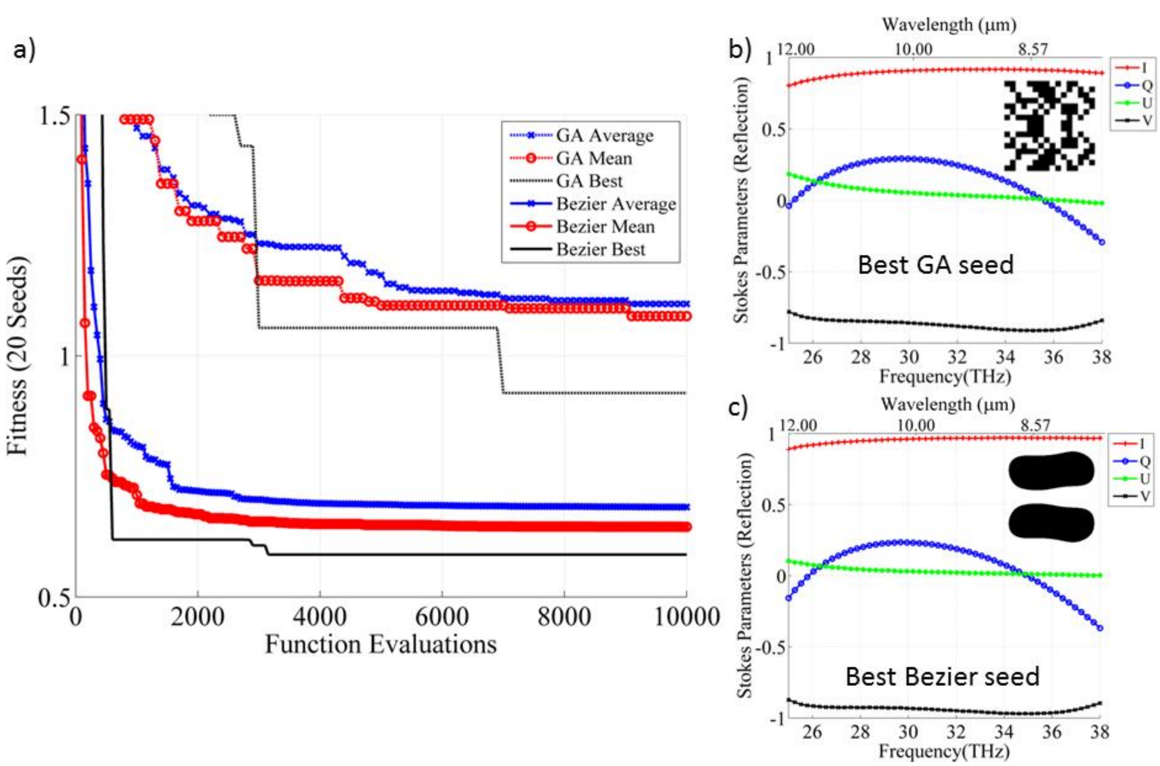

Figure 3.4. Performance comparison of pixelated structure GA optimizations versus Bézier surface CMA-ES optimizations. (a) Mean, median, and best fitness over 20 seeds for GA and CMA-ES optimizations. (b) Dispersive Stokes parameters for the best GA optimized seed. (c) Dispersive Stokes parameters for the best Bézier surface seed.

3.2.2 Performance Comparisons Between Reconfigurable Bézier Surfaces and the Split-ring Geometry

In this section, the performance of a reconfigurable Bézier metasurface is compared to the reconfigurable split-ring metamaterial structure from Figures 2.11–2.13. The *I* and *V* Stokes parameters are shown plotted in Figure 3.5 for both the SR and Bézier metasurfaces. It can be seen that the optimized Bézier metasurface provides a higher intensity as well as a broader band quarter-wave response. The unit-cells of the respective structures are depicted in the insets. The SR unit-cell is 975 nm by 975 nm and the SR itself is comprised of 150 nm thick Au supported by a 465 nm GST substrate that is backed by a 150 nm Au ground plane. The Bézier unit-cell is 1300 nm by 100 nm (a square 1 by 13 unit-cell array is shown in the inset for Figure 3.5) and is comprised of 150 nm thick Au supported by a 500 nm GST substrate that is backed by a 150 nm Au ground plane.

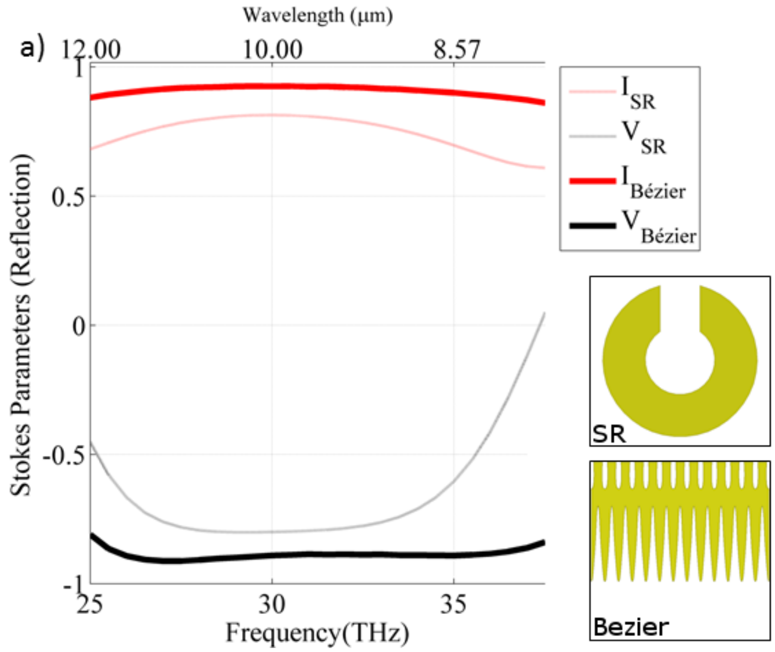

Figure 3.5. Dispersive Stokes *I* and *V* parameters comparing the SR's CP response versus that of the optimized Bézier metasurface.

3.2.3 Additional Examples of Bézier Metasurfaces

In this section, additional optimized Bézier metasurfaces operating in the MWIR and LWIR are presented. Specifically, a multi-octave splitter and half-wave and quarter-wave metasurfaces operating at MWIR are presented.

3.2.3.1 Multi-Octave Infrared Linearly Polarized Splitter

The first design is an optimized linear polarization splitter. The Bézier surface is optimized to scatter ±*U*-polarized waves across the MWIR and LWIR bands (3 µm to 15 µm). The performance of the final design is presented in Figure 3.6 where the MWIR and the 8 µm to 12 µm atmospheric transmission band are highlighted. The optimized design exhibits a multi-octave response spanning 3µm to 15µm (i.e. MWIR to LWIR). The synthesized unit-cell for the 2-D periodic structure measures 2300 nm by 300 nm and consists of a 75nm Au layer deposited on top of a 50nm layer of SiO_2. A depiction of a 1 by 5 unit-cell section is shown in the inset of Figure 3.6. The scattering as a function of azimuthal rotation is shown in Figure 3.7.

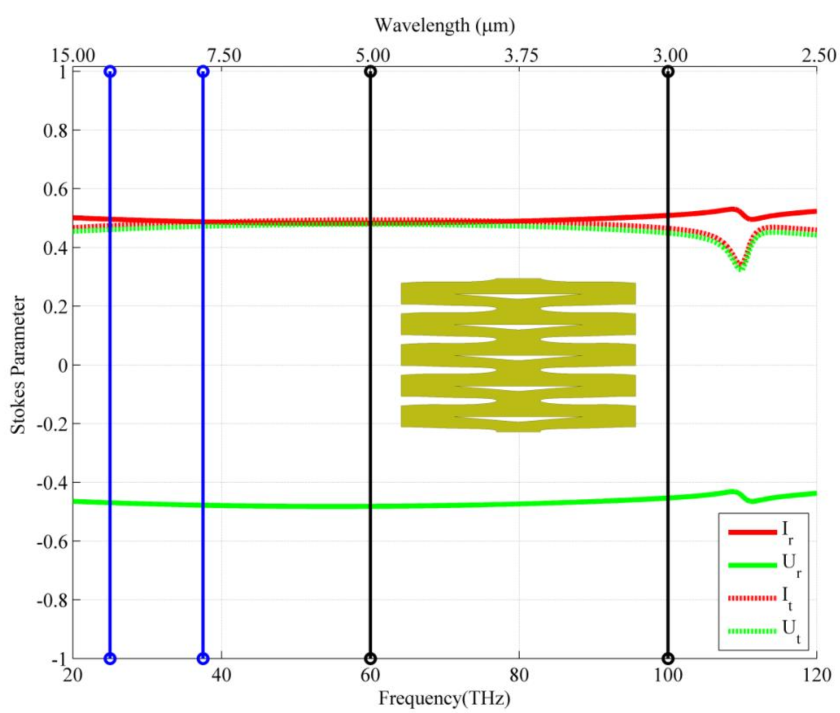

Figure 3.6. Pertinent Stokes parameters for the scattering of a Bézier linear polarized splitting metasurface spanning MWIR to LWIR.

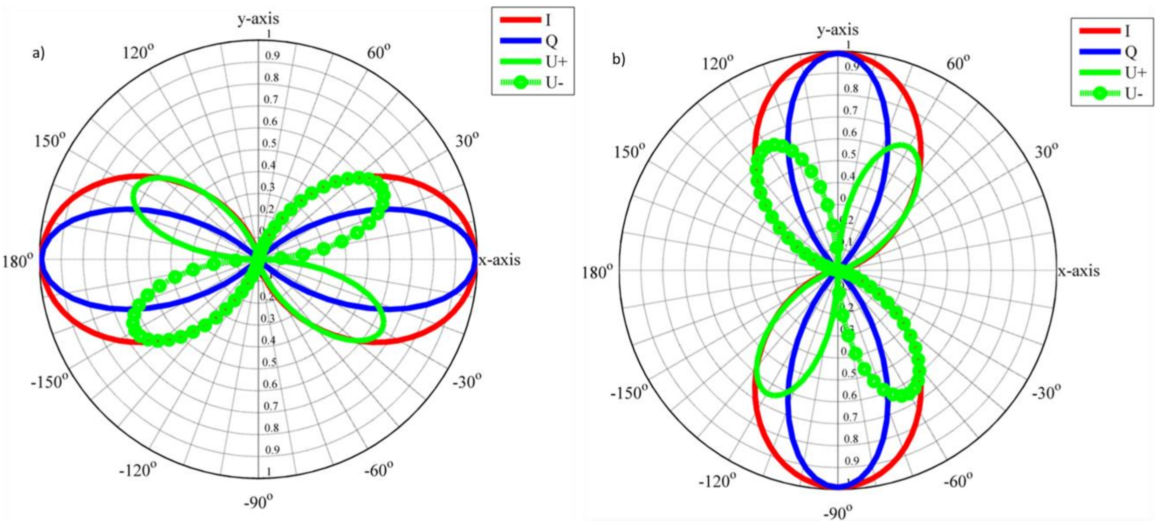

Figure 3.7. Stokes parameters as a function of azimuthal rotation for (a) reflection and (b) transmission of Bézier splitter.

3.2.3.2 Mid-Wavelength Infrared Half-Wave Plate

Next, a half-wave plate Bézier metasurface is optimized to cover the 3 µm to 5 µm band. The optimized Bézier unit-cell is 1700 nm by 1550 nm. The surface is comprised of a 150 nm thick patterned Au layer supported by a 650 nm SiO_2 substrate that is backed by a 150 nm Au ground plane. The results are illustrated in terms of pertinent Stokes parameters in Figure 3.8(a), and the azimuthal response is shown in Figure 3.8(b). These results demonstrate an *extremely* wide band half-wave response that surpass the desired 3 μm to 5 μm range and compare favorably to results presented in other work [81].

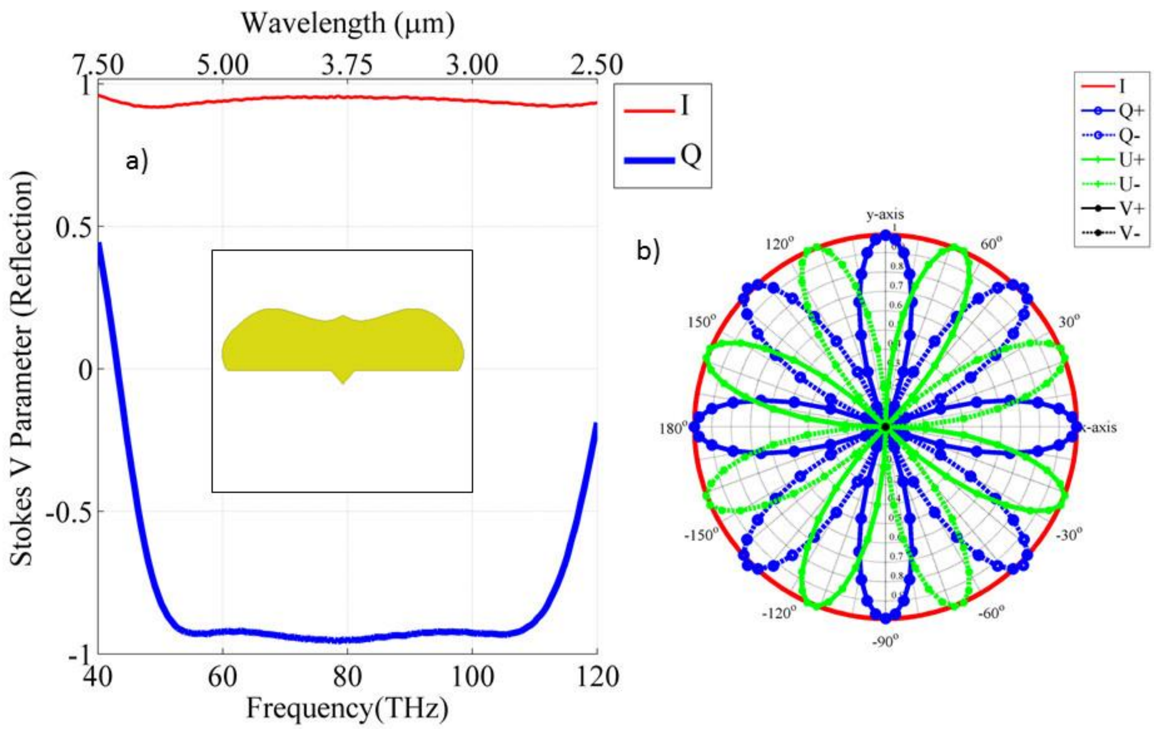

Figure 3.8. Bézier half-wave metasurface MWIR response at (a) normal incidence and (b) in-band azimuthal response.

3.2.3.3 Mid-Wavelength Infrared Quarter-Wave Plate

Finally, a quarter-wave plate Bézier metasurface is optimized to cover the 3 μm to 5 μm band. The optimized Bézier unit-cell is 2050 nm by 200 nm (a square 1 by 10 unit-cell array is shown in the Figure 3.9 (a) inset). The surface is comprised of a 150 nm thick layer of patterned Au, supported by a 370 nm SiO_2 substrate, and then backed by a

150 nm Au ground plane. The results are displayed in terms of pertinent Stokes parameters in Figure 3.9(a), and the azimuthal response is shown in Figure 3.9(b). The results once again demonstrate an *extremely* wide band quarter-wave response, far surpassing the targeted 3 µm to 5 µm range.

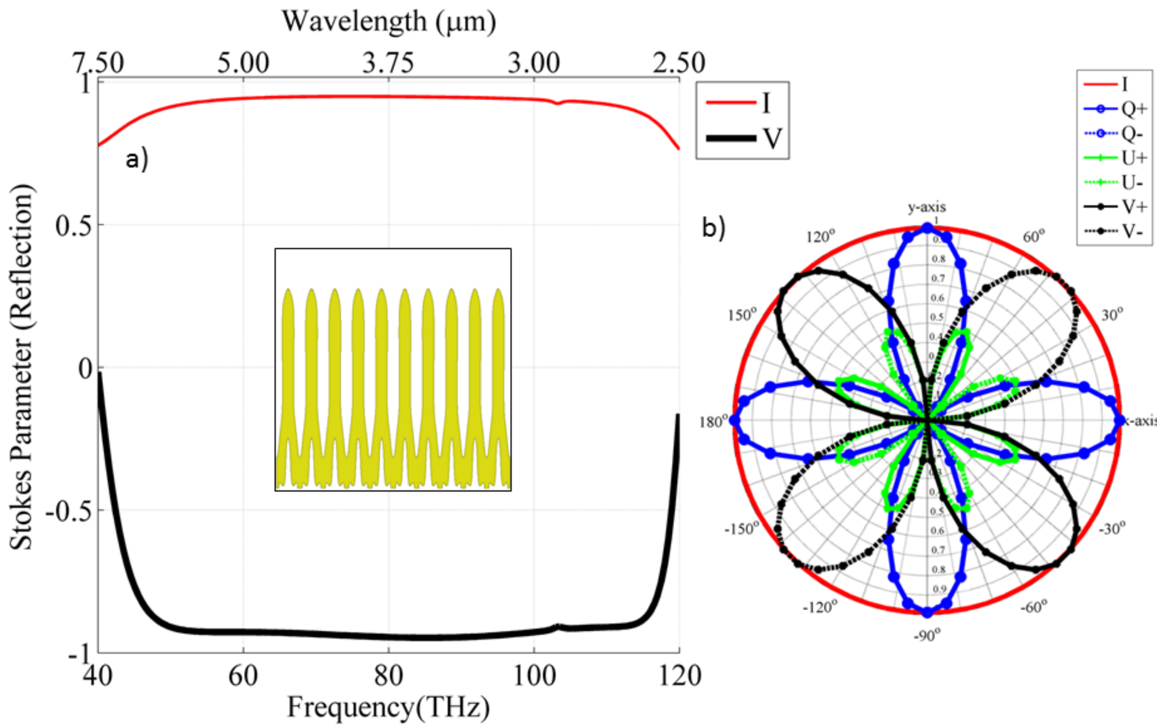

Figure 3.9. Bézier quarter-wave metasurface MWIR response at (a) normal incidence and (b) in-band azimuthal response.

Chapter 4

A Dual-Band Circularly Polarized Microstrip Patch Antenna Demonstrating Reconfigurablity

4.1 Reconfigurable Patch Antennas

Patch antennas are prevalent in literature and a popular choice for antenna designers of antennas that operate at high frequencies. They are low-profile, relatively simple, and inexpensive to manufacture. This makes them a desirable option at shorter wavelengths. In its simplest form, a linearly polarized patch antenna excites the TM_{10} mode at a frequency for which the patch's length equals $\lambda_{eff}/2$. Circular polarization is achieved by exciting the TM_{10} and TM_{01} modes through the introduction of the appropriate asymmetries [55]. In addition, multi-band behavior can generally be introduced by the inclusion of properly designed slots. However, it is not a given that the radiation patterns for each frequency will be well behaved. This is due to the fact that such designs often operate by exciting higher order modes which can result in undesired lobes in the radiation patterns. Additionally, relying on higher order modes also fundamentally limits how small the frequency ratio between bands can be.

A popular design that satisfies the criteria for dual band circular polarization with a small frequency ratio and well behaved radiation patterns is the stacked patch antenna.

However, its multilayer design and a general desire for size reduction calls for further investigation into the problem. Moreover, the integration of reconfigurability would further increase the utility of such an antenna. As such, this work presents a miniaturized, dual-band, circularly polarized, conformal and reconfigurable patch antenna.

4.1.1 End-Loading

A useful alternative to exciting higher order modes for multiband behavior is the use of reactive end-loading. Reactive end-loading relies on terminating a micro strip transmission line with a significantly mismatched load. The load is often chosen to be a short, or, in the case of reconfigurable designs, a variable capacitor terminated to ground. This length-dependent transmission line excites a secondary resonance when the transmission line length corresponds to $\lambda_{eff}/2$, thereby shorting the edge of the patch. Yet, it can also be recognized that a more compact resonant structure exists which can achieve a frequency dependent short at the patch edge.

First, a study is conducted on a proposed custom metamaterial end-load. The composite structure, shown in Figure 4.1(a), consists of a dipole end-load surrounded by a ring. The individual structures are compared in terms of input impedance. The metric used to assess performance is the spacing and location of the resonance zero-crossings where closely spaced zero-crossings occurring at a low frequency is optimal. From the results in Figure 3.1(b), we can see that the dipole end-load has a relatively low Q-factor resonance resulting in a high resonance frequency outside of the band of interest and only one zero crossing within the band of interest. The ring, on the other hand, displays a higher Q-factor and contains two zero-crossings within the plotted band. Unfortunately, the spacing of the zero-crossings is far too wide for our application, since the zero-crossings need to occur well within one octave. This ensures the excitation of a degenerate fundamental mode rather than an undesirable (from a radiation pattern standpoint) higher order mode. Finally, the composite structure which combines the two aforementioned geometries into a single resonator through coupling does exhibit the desired zero crossing location and spacing and is subsequently used in the proceeding patch antenna design.

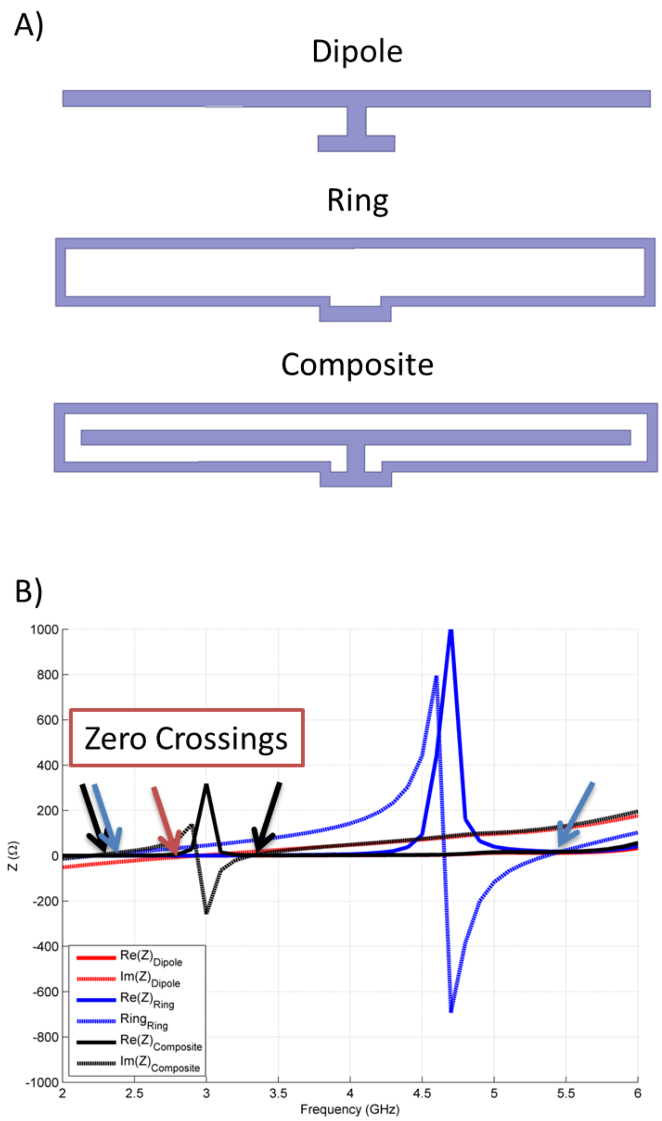

Figure 4.1. a) Depiction of the dipole, ring, and composite end-load structure. b) Input impedance of each structure.

The geometry of the patch antenna integrated with the end-loads is depicted in Figure 4.2. This patch, properly matched to a probe feed, will radiate at the two zero-crossings designated by black arrows in Figure 4.1. However, to further increase the utility of the design, the design is expanded into a circularly polarized dual band patch. This is achieved by adding end-loads along the orthogonal edges, thereby exciting the TE_{10} mode. To facilitate the desired 90° phase shift between these orthogonal modes, a slot is introduced into the center of the patch to perturb the currents that create a phase difference between the orthogonal modes. The geometry and the currents for the final circularly polarized design are depicted in Figure 4.3 for the degenerate mode. From the current distribution, we can see that the end-loads do in fact create a short at the end-load termination along the patch edge.

Figure 4.2. Geometry of the end-loaded patch antenna.

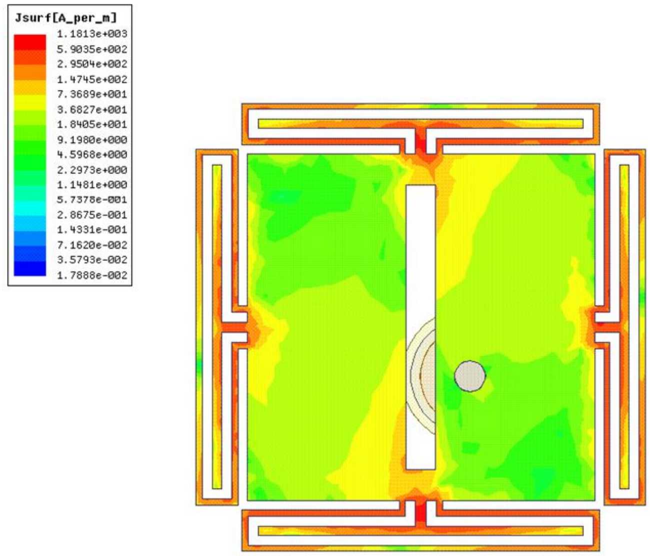

Figure 4.3. Currents of the end-loaded circularly polarized patch antenna for the degenerate mode resonance.

The performance of this circularly polarized dual band patch antenna is summarized in Figure 4.4. The S_{11} is shown in Figure 4.4(a). The total gain, the total realized gain, the left hand circularly polarized (LHCP) realized gain, and the right hand circularly polarized (RHCP) realized gain are depicted and Figure 4.4(b). Furthermore, the isotropic radiation patterns for the fundamental and the degenerate mode resonances are shown in Figure 4.5. From these results, we can conclude that the antenna preforms well, exhibiting dual fundamental radiating modes as expected.

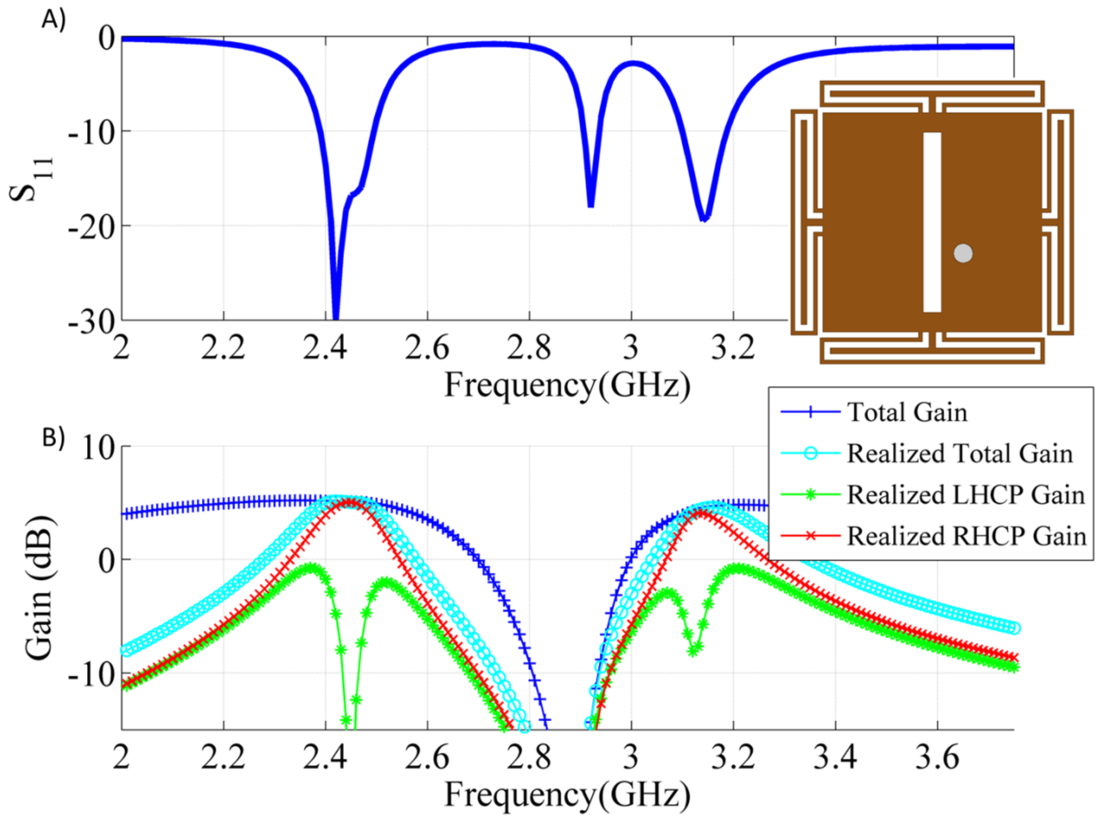

Figure 4.4. a) S_{11} of a dual band circularly polarized patch antenna (inset: patch geometry). b) Total gain, realized gain, and realized LHCP and RHCP gain.

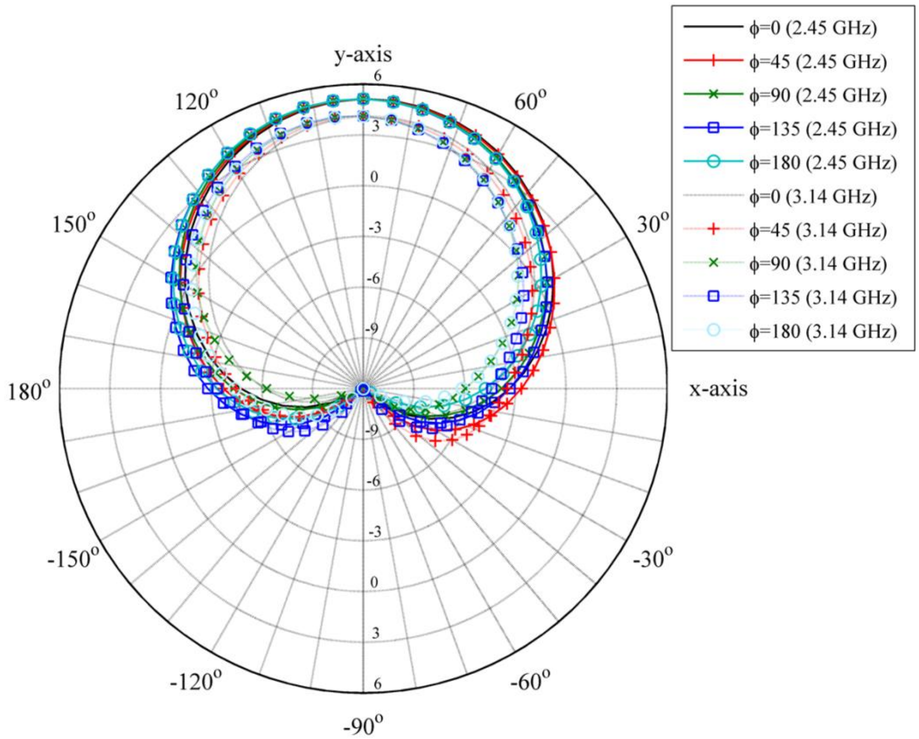

Figure 4.5. Azimuthally dependent realized gain for both frequency bands.

4.1.2 Introducing Reconfigurability

As previously mentioned, a metamaterial can be made to be reconfigurable at RF frequencies by changing either the capacitance or the resistance of the equivalent circuit. Using the dual band patch described in the previous section, reconfigurability is demonstrated for either varying capacitance or varying resistance. Referencing Figure 4.6, two different configurations for a capacitively reconfigurable and a restively reconfigurable design are presented. For the capacitive approach, the appropriate port placement is depicted in Figure 4.6(a). Such a variable capacitance can be achieved by the use of an active component such as a varactor or MEMS, assuming the proper biasing is accounted for. Next, the port placement for the resistively reconfigurable design is depicted in Figure 4.6(b). This switching can be achieved by an active component such as an RF switch or by the incorporation of a ChG PCM switch (discussed in more detail in the proceeding chapter).

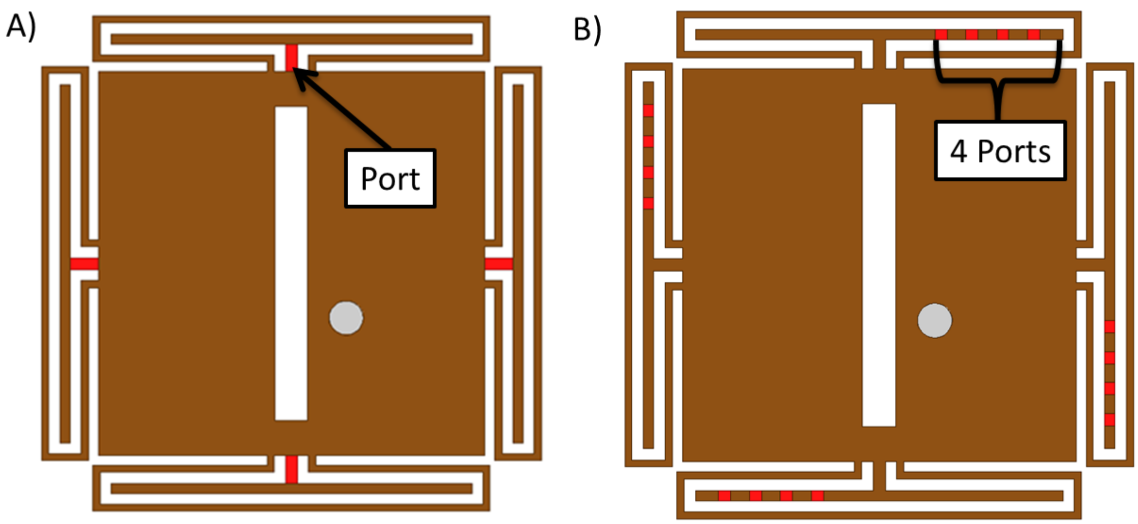

Figure 4.6. a) Port location for capacitively controlled reconfigurability. b) Port location for resistively controlled reconfigurability.

The S_{11} response of the capacitively reconfigurable design is shown in Figure 4.7. The fundamental resonance remains stationary for all states whereas the degenerate mode is influenced by a change in port capacitance. An open and a short define the bandwidth bounds of the reconfigured design, and four capacitance values ranging from 0.7 pF to 2.9 pF are shown to provide discernible frequency shifting within that band.

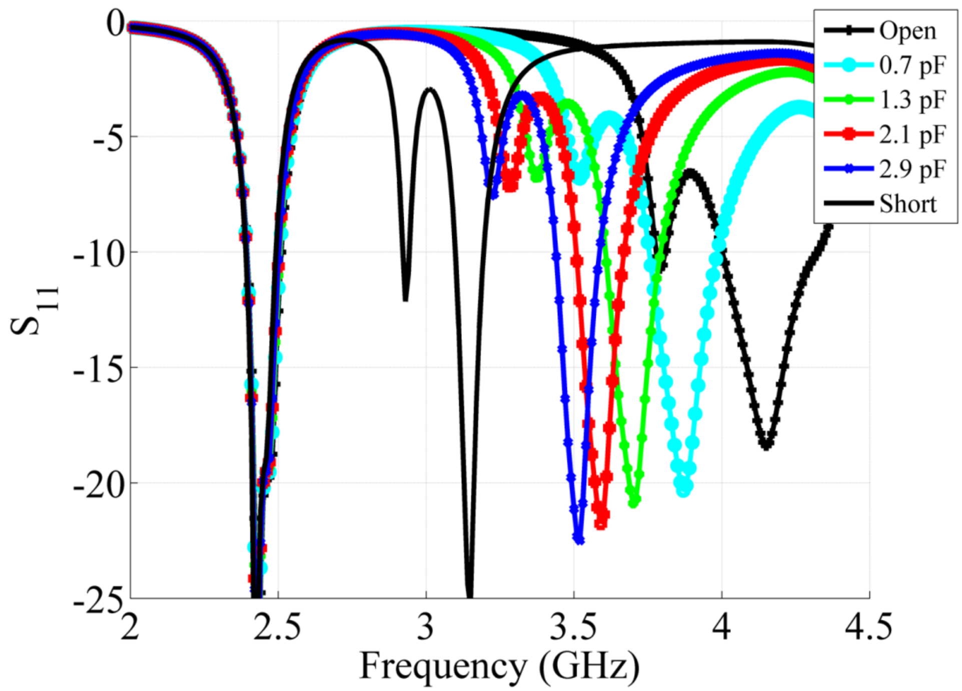

Figure 4.7. S_{11} as a function of capacitance for the reconfigurable design shown in Figure 4.6(a).

Finally, the S_{11} response of the resistively reconfigurable design is shown in Figure 4.8. Noting the change in port placement, the fundamental resonance once again remains stationary for all switch states whereas the degenerate mode is influenced by a change in dipole length of the composite metamaterial end-load, which is controlled by opening or shorting the ports as noted in Figure 4.8.

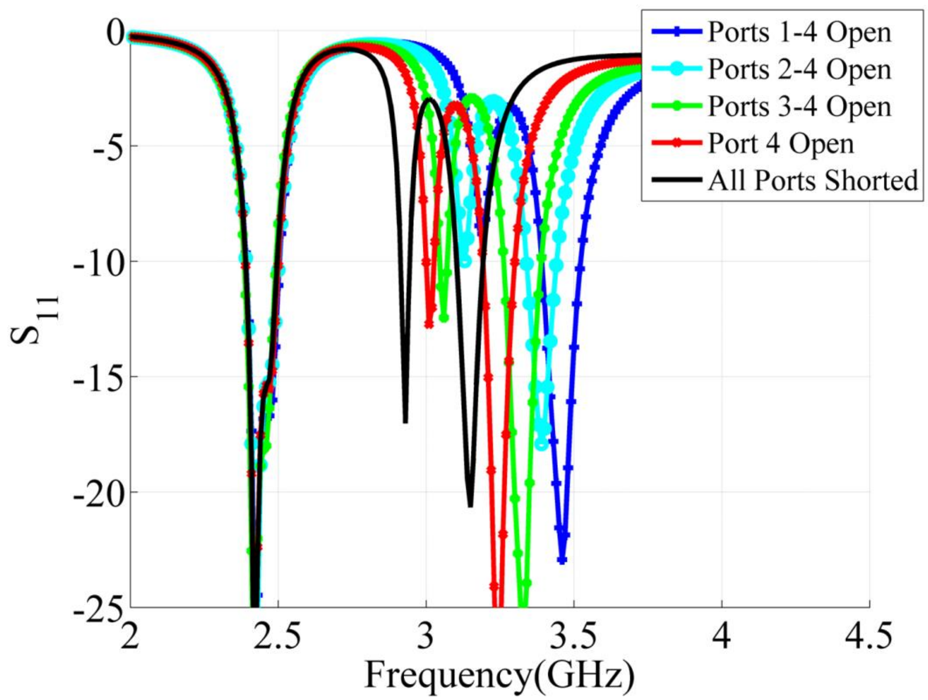

Figure 4.8. S_{11} as a function of shorted ports for the resistively reconfigurable design described in Figure 4.6(b).

Chapter 5

Characterization of an RF Switch Based on Chalcogenide Glass Phase Change Materials

5.1 The History of Chalcogenide Glass Phase Change Materials and the Beginnings of Solid State Memory Storage.

In the early 1900s, Alan Tower Waterman of Yale University observed that the conductivity of the chalcogenide MoS_2 behaved in a strange manner [140]. Specifically, he observed that Ohm's law was not obeyed, demonstrating a negative coefficient of resistance with respect to temperature [140]. This behavior is now known to be typical of semiconducting chalcogenide materials. Waterman noted that a breakdown in resistance occurred when the material was heated by an electrical current and subsequently noted that the material can exist in two forms, both high and low conductivity [140]. In 1962, A. David Pearson of Bell Laboratories reported that the high and low conductivity states were reversible given the appropriate electrical pulses [140]. In 1968, Stanford Ovshinsky demonstrated that this switching could be done many times, thereby laying the foundation for phase change memory [140, 141]. Subsequent patent filings noted that the "set" operation require that an applied voltage must exceed a threshold value and that the "reset" is a melt-quench process which requires a rapid removal of applied voltage [140]. The limiting factor at the time was that the amount of energy needed to switch these 10 μm films was prohibitive. However, as semiconductor devices were scaled down over the next several decades so did the ability to scale down the ChG films to ~100nm which resulted in a significant reduction in switching power consumption.

5.2 The Kinetics of Chalcogenide Glass Phase Change Materials.

Contrary to the work done at RF using a PCM VO_2, whose resistance changes linearly as a function of temperature (ignoring a slight hysteresis) [151-153], ChG PCMs RF switches offer an inherent advantage in that they are bistable (i.e. either permanently off or on), as is the case with any ideal switch. In this section, an alternative to known RF switching technologies is investigated for integration into RF devices. This material is the chalcogenide (ChG) based phase change material $Ge_2Sb_2Te_5$ (GST). This class of phase change materials (PCMs) has the potential to provide large changes in RF conductivity (rather than permittivity changes). As a result, the equivalent circuit of an RLC metamaterial can be changed in terms of resistance. As will be demonstrated in Chapter 6, these drastic conductivity changes can be exploited to design novel reconfigurable metamaterial devices.

The change in resistivity for such ChG PCM materials occurs when they undergo a thermally driven phase transition from an amorphous glass to a crystalline semi-metal, which results in large changes in both the optical and electrical properties of the material. Based on these profound property changes, PCMs such as GST have been integrated into a variety of commercially available optical disks and electrically addressed, nonvolatile memory products. While the material properties of GST are well known at DC and optical wavelengths, nothing had been reported characterizing GST at RF until 2011 [135].

5.2.1 Crystallization Kinetics and Amorphizing Energy by Optical Energy

Glassy materials are produced by the rapid supercooling of a liquid below its melting point to a temperature at which the atomic motion necessary for crystallization cannot occur [145]. This process is exploited in ChG-based PCM switch, whereby controlling the input energy intensity and pulse duration, a PCM switch can be changed between the amorphous and crystalline states. The crystallization kinetics of a 140 nm thick film of a chalcogenide, $Te_{77}Ge_{20}As_3$, is studied using a laser source [143]. The transmission ratio,

$$\frac{I_{trans}}{I_{inc}}, \tag{5.1}$$

gives the intensity ratio of the transmission of incident beam into the sample relative to the transmission exiting the test sample. Given a film thickness, d = 140 nm, Equation 5.1 can be expressed as

$$\frac{I_{trans}}{I_{inc}} = f(e^{-\Delta\alpha d}) + (1 - f)$$

(5.2)

where f is the crystallization fraction and $\Delta\alpha$ is the difference between the absorption constants between the crystalline and amorphous regions. Equation 5.2 shows that f is directly proportional to unity subtracted by the transmission ratio. In other words, a reduction in absorption signifies a higher degree of crystallization, and, more importantly a higher beam intensity results in a higher degree of crystallization. Therefore, the rate of crystallization, given as:

$$\frac{d(f)}{dt} \propto \frac{d\left(\frac{I_{trans}}{I_{inc}}\right)}{dt}$$

(5.3)

also states that the higher the incident field intensity the *faster* the crystallization process. From the crystalline state, the chalcogenide can be returned to the amorphous state using

$$\mathrm{P} \approx L\frac{d(x)}{dt}$$

(5.4)

where P represents the applied power, L corresponds to the heat of fusion, and x refers to the distance of the melt line to the surface. In other words, more incident power results in a faster melt rate. It is assumed that upon rapid removal of the power source, a substrate with a high thermal conductivity results in rapid quenching of the PCM. Further work on the kinetics of optically excited GeTe-based alloys also demonstrated a similar behavior [167].

5.2.2 Crystallization Kinetics and Amorphizing Energy from an Electrical Source

More recent work has focused on $Ge_2Sb_2Te_5$ (GST) in which the phase change is facilitated through electronic pulses [144-147]. For crystallization, the amorphous material must be heated to a temperature between these two temperatures for a sufficient amount of time (see Figure 5.1). When a particular threshold voltage, V_{th}, is exceeded, the material rapidly changes into a highly conductive state. Once the current passes for a significant amount of time, the crystallization is set [145]. The PCM can in turn be reset by a short higher voltage pulse. To reset, the pulse needs to have a sufficient magnitude and duration to melt the PCM, in addition to having a fast enough falling edge to permit rapid cooling [145]. The specific amplitudes and durations of the set and reset pulses are contingent on the amount of bulk material and resultant thermodynamics of the switch geometry.

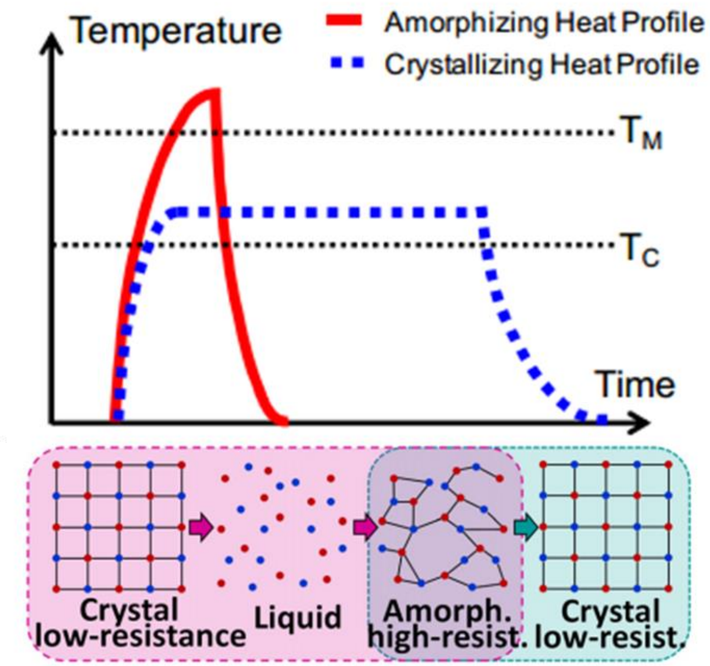

Figure 5.1. Depiction of heat needed to switch a PCM to the amorphous and crystalline states respectively.

5.3 Properties of Chalcogenide Glass Phase Change Materials at Radio Frequencies

5.3.1 Mismatched Transmission Line Test Cell

In order to characterize GST at RF, a test setup was devised. A coplanar waveguide (CPW) to be measured at 10 GHz to 50 GHz was designed. Usually, by the use of analytic equations, a micro strip transmission line (TL) is engineered to match the characteristic impedance of the probe station (50 Ω). The subsequent insertion loss is used to characterize the material under test. However, testing had to be compatible with fabrication techniques and materials necessary to adhere a 250 nm layer of GST to the TL. Specifically, the quartz substrate measured 1.575 μm with an almost 20% tolerance on thickness between samples. The tolerance on thickness can result in an obvious problem when engineering a micro strip transmission line for the prescribed characteristic impedance. Additionally, since the probe station platform was grounded, the analytical solution for a CPW backed by a ground plane breaks down due to the substrate thickness. Conversely, using the analytical solutions for a CPW without a ground plane is not advisable since the ground plane is still very much within the near field. Lastly, the TL traces consist of a 500 nm film of gold (Au) which was on the order of its skin depth. Again, analytical solutions for RF designs assume a 2-D conductive surface (i.e. a thickness of at least 5x the skin depth). As a result, the field distribution and the attenuation constant of the TL line also differ from the analytical solutions.

Rather than relying on potentially inaccurate analytical models for a microstrip TL, a custom test structure that was tolerant to slight impedance mismatches was devised using a CPW TL structure that was designed parametrically using a full-wave solver. The structure shown in Figure 5.1(a) is used to characterize the conductivity of GST in the amorphous and crystalline states. Before crystallizing the GST, the CPW TL sees an open circuit for an electrical length of 2.5 mm. After the GST is crystallized, the length of the transmission line doubles to 5.0 mm. The return loss of the CPW TL can be used to verify switching behavior because an impedance match occurs when the GST becomes sufficiently conductive as the TL is loaded by a second probe with a $Z_{load} = 50\ \Omega$. Since there is some mismatch between the loads and the TL characteristic impedance, the best impedance match condition occurs at ~ 19 GHz and ~ 38 GHz for the conductive GST states, which corresponds to a half-wave impedance transformer. Conversely, when the GST is not sufficiently conductive, the input of the TL sees the input impedance depicted in Figure 5.1(b). The simulated and measured responses are shown in Figure 5.2. By comparing the data, we can extract the conductivities for GST in the amorphous and crystalline states as 100 S/m and 100k S/m, respectively.

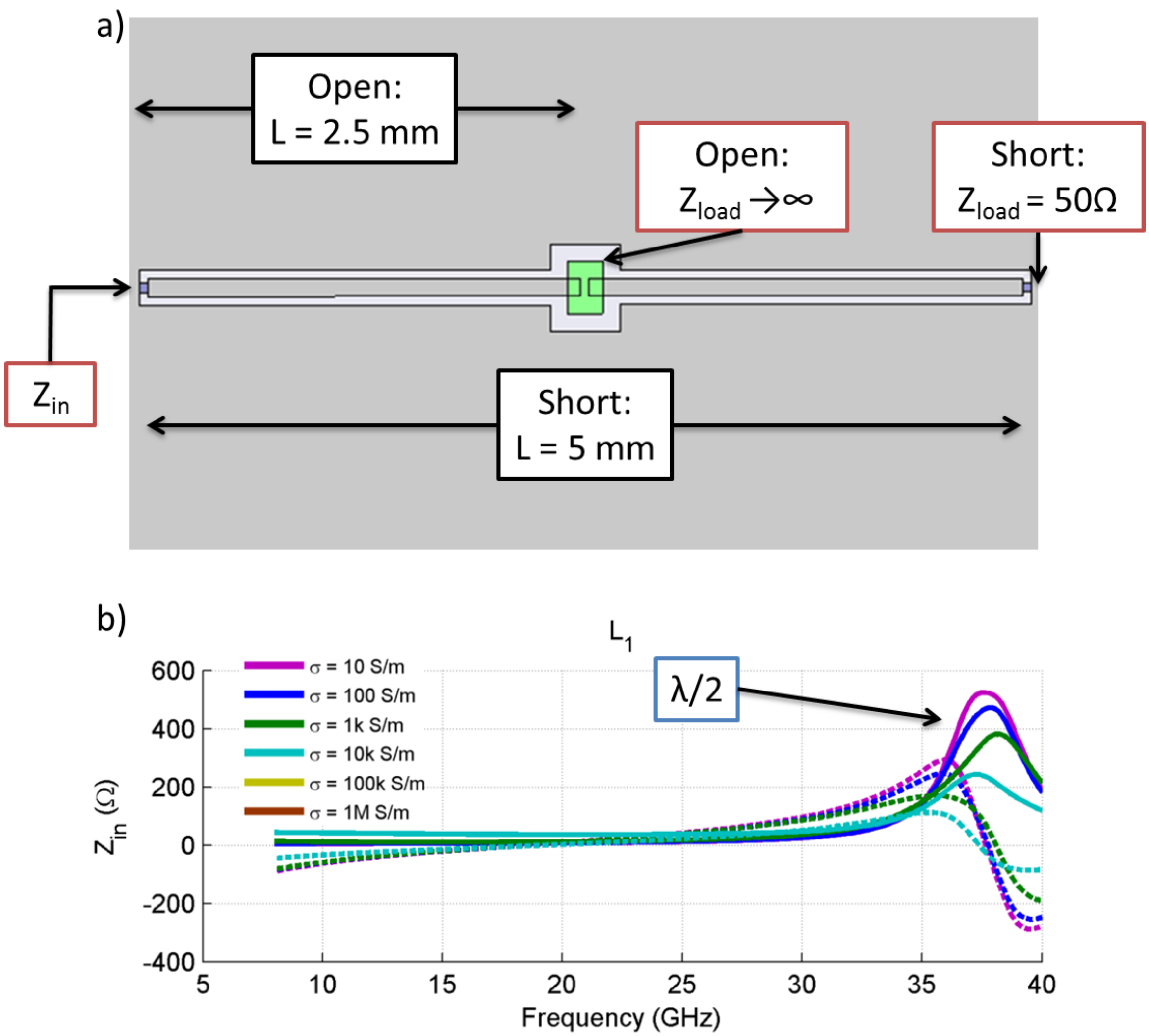

Figure 5.1. a) Transmission line test cell with GST in the center. b) Input impedance as a function of GST conductivity.

a)

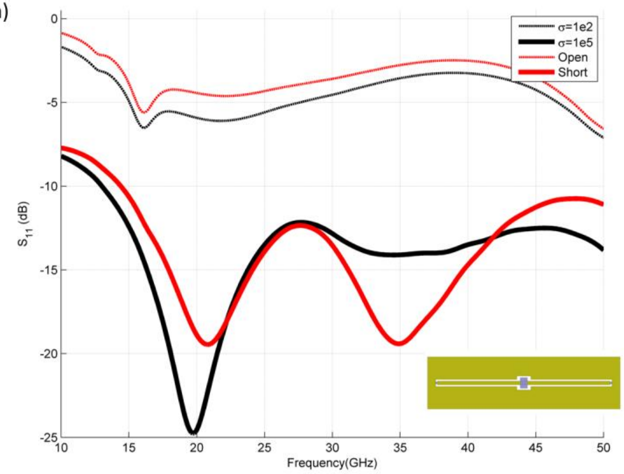
σ=1e2
σ=1e5
Open
Short
S11 (dB)
Frequency(GHz)
0
-5
-10
-15
-20
-25
10
15
20
25
30
35
40
45
50

b)

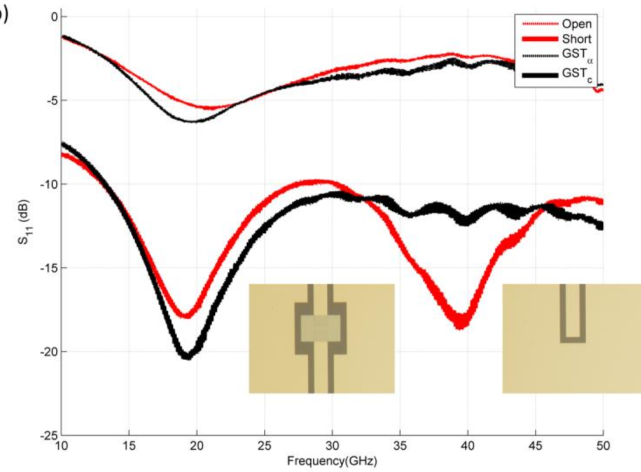
Open
Short
GSTα
GSTc
S11 (dB)
Frequency(GHz)
0
-5
-10
-15
-20
-25
10
15
20
25
30
35
40
45
50

c)

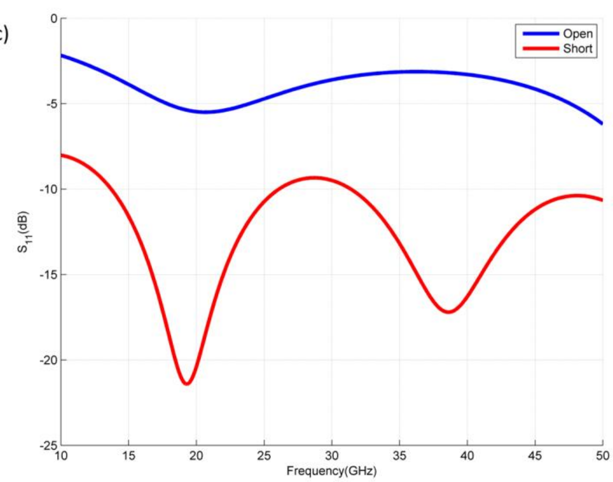
Open
Short
S11(dB)
Frequency(GHz)
0
-5
-10
-15
-20
-25
10
15
20
25
30
35
40
45
50

Figure 5.2. a) Simulated S_{11} for ideal open and short transmission lines compared to fitted GST conductivity (inset: modeled structure). b) Measured transmission line response for GST in the amorphous and crystalline states compared to an ideal open and short (inset: fabricated structure GST section and a probe pad, respectively). c) The simulated transmission line response for GST in the amorphous and crystalline states compared to an ideal open and short, accounting for non-ideal probe placement due to ‘skating’.

5.3.2 GST in Waveguide Test Cell

For confirmation, the conductivity for both GST phases was tested in a different configuration. In this particular configuration, a 300 nm layer of GST was deposited on a quartz slide. In the amorphous state, the GST slide should be almost transparent, causing the scattering parameters of the waveguide to remain mostly unchanged. When the GST is in the crystalline state its conductivity creates a short, preventing the wave from propagating across the waveguide. Referencing Figure 5.3, it is clear from the simulated and the measured response that a large, broadband conductivity contrast exists between the amorphous and crystalline states. The extracted conductivity values for GST in the amorphous and crystalline states are again shown to be 100 S/m and 100k S/m, respectively.

a)

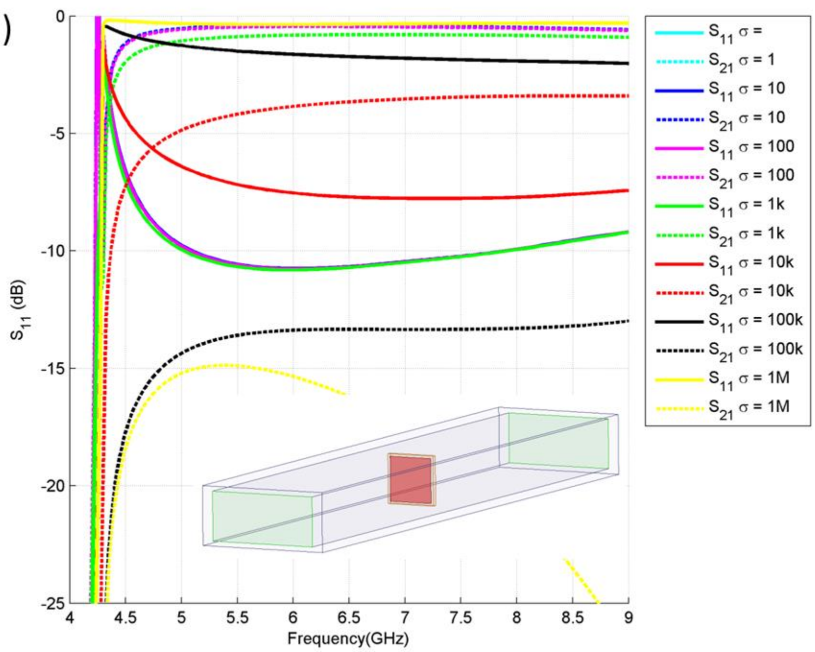
S11 (dB)
Frequency(GHz)
S11 σ =
S21 σ = 1
S11 σ = 10
S21 σ = 10
S11 σ = 100
S21 σ = 100
S11 σ = 1k
S21 σ = 1k
S11 σ = 10k
S21 σ = 10k
S11 σ = 100k
S21 σ = 100k
S11 σ = 1M
S21 σ = 1M

b)

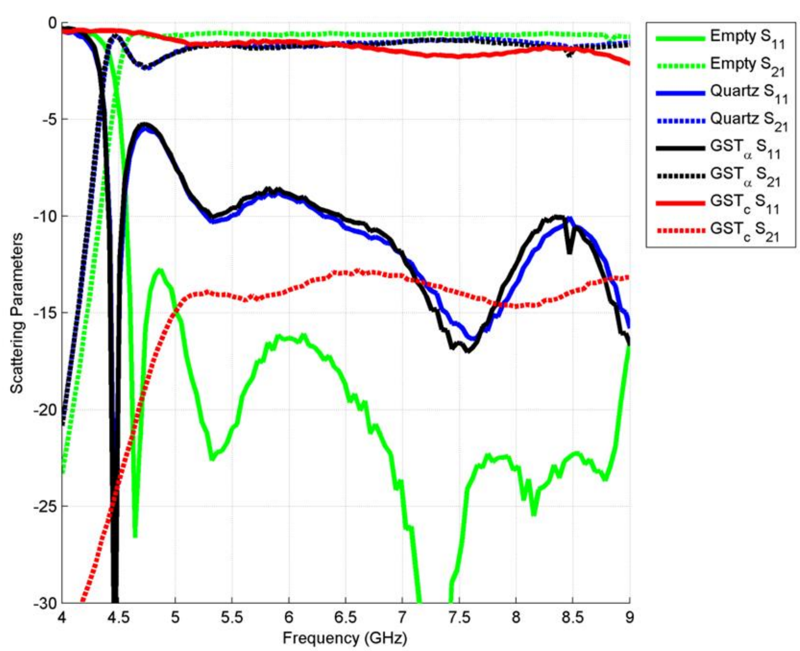
Scattering Parameters
Frequency (GHz)
Empty S11
Empty S21
Quartz S11
Quartz S21
GSTα S11
GSTα S21
GSTc S11
GSTc S21

Figure 5.3. a) Simulated rectangular waveguide response as a function of GST conductivity (inset: rectangular waveguide loaded with GST test cell). b) Measured rectangular waveguide response for amorphous and crystalline GST.

5.3.3 A High Performance Four Terminal Bistable PCM Based RF Switch

The cut-off frequency for any RF switch is related to the on state resistance and the off state capacitance given as [115]

$$f_c = \frac{1}{2\pi R_{on} C_{off}}. \tag{5.5}$$

Similarly, a figure of merit [135],

$$\mathrm{FOM} = \frac{Z_{on}}{Z_{off}} = j\omega R_{on} C_{off}, \tag{5.6}$$

is used to assess the dispersive on/off ration of the switch. Using typical values for a pin diode, MEMS, and measured values for ChG PCM switches [115, 135], the FOM is converted to transmission referencing a typical 50 Ω RF system [17]. From Figure 5.4, we observe a superior on/off ratio and bandwidth for the ChG PCM switch.

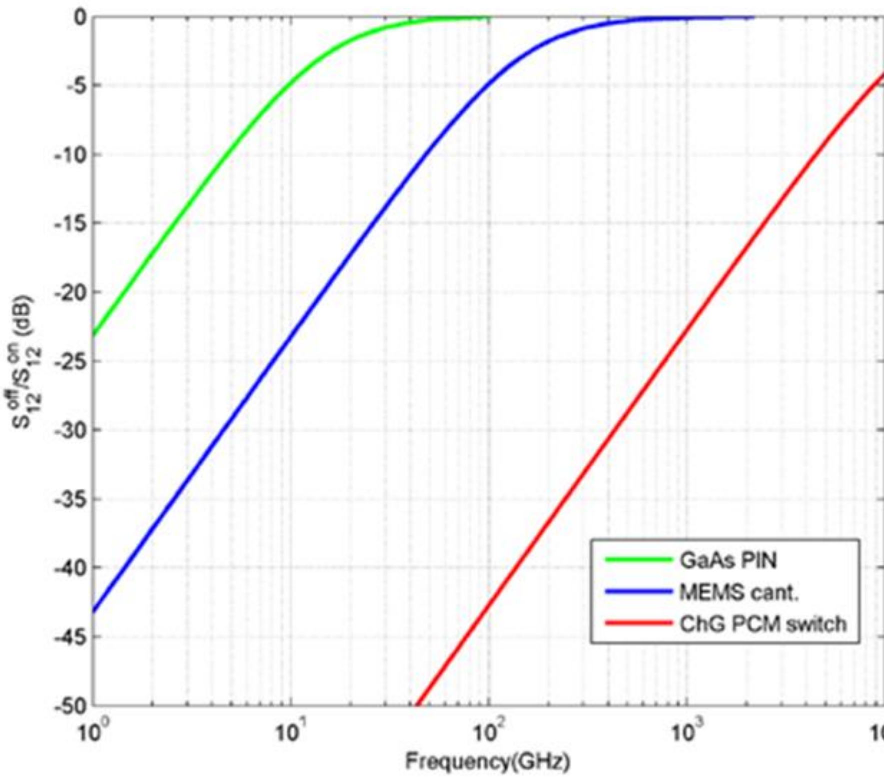

Figure 5.4. Figure of merit for using typical and measured values for a PIN diode, MEMS, and ChG PCM switch.

Subsequent work has characterized ChG PCM RF switches [153-159]. These authors elected to use GeTe rather than GST; although, tthe reason for using GeTe rather than GST isn't clear because GeTe exhibits a higher melting temperature of ~190°C [154] compared to ~150°C for GST. A realized heater structure was fabricated (Figure 5.5) and measurements were conducted. The extracted on state resistance (tenths of Ohms) and off state capacitance (on the order of femto farads) in [153, 154] are similar to those given by the extracted conductivity values from [135], varying only slightly due to slight differences in RF contact geometry [153, 154]. Using these results the return loss (S_{11}) and the insertion loss (S_{12}) are plotted in Figure 5.6. Finally, the switching behavior of the RF switch is studied in [156] and a thorough thermodynamic analysis of the heater stricter is covered in [158]. The switching behavior is depicted in Figure 5.7, where the on to off switching is achieved with a 100 nS pulse, consuming 1.55 W, and the off to on switching is achieved with a 1500 nS pulse, consuming 0.5 W [156].

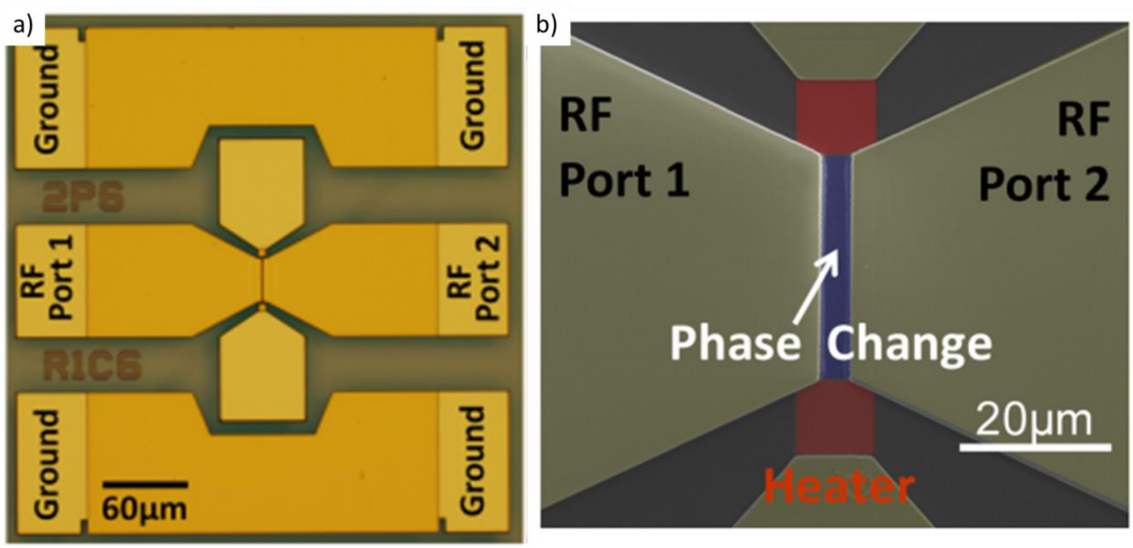

Figure 5.5. a) Phase change switch test cell with RF ports and DC heater ports. b) Close-up colorized SEM image of a phase change switch [156].

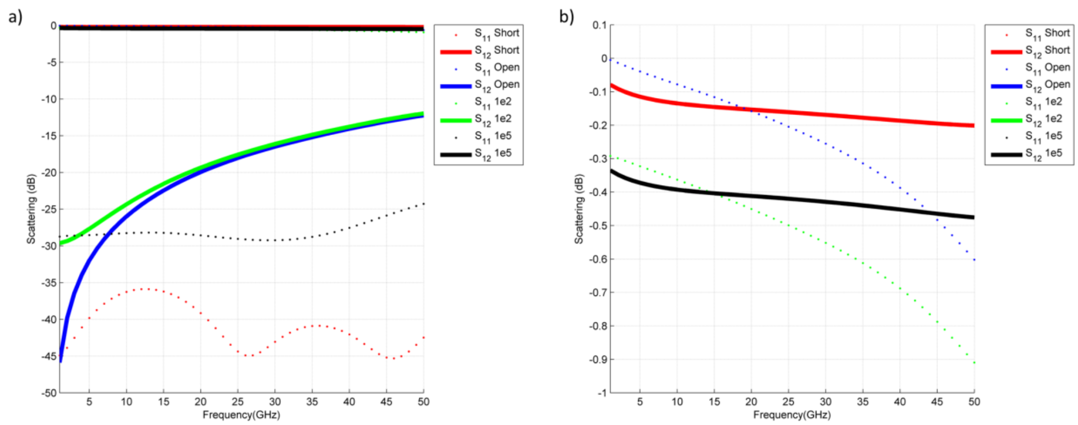

Figure 5.6. a) S_{11} and S_{12} of an open and shorted micro-strip compared to GST conductivities. b) Close-up of data to assess insertion loss.

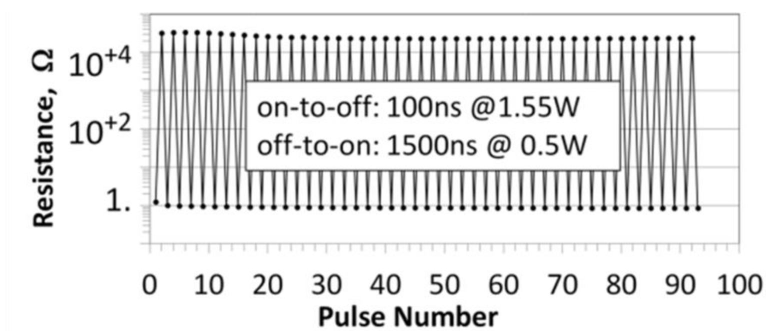

Figure 5.7. Pulse duration and power consumption of state switching for a GeTe based RF switch [156].

Chapter 6

A Multi-Band, Multi-State Frequency Selective Surface Using an RF Switched Based on a Chalcogenide Glass Phase Change Materials

In this chapter, a novel reconfigurable FSS structure inspired by the metamaterial is used to end-load the patch antenna described in Chapter 4. A ChG PCM RF switch, exhibiting the properties discussed in Chapter 5, is used to facilitate the switching. Additionally, the necessary bias lines are integrated into the metamaterial design. The metasurface can be configured into four unique states within the X-band (8 GHz to 12 GHz). Specific frequency channels are used for sensing each state. They behave as a spectral barcode, effectively sensing four distinct states using a combination of reflection and or transmission at these three channels (analogous to the absorbing and reflecting lines found in a barcode).

In Figure 6.1, the unit-cell for the quad state FSS is depicted. DC lines that carry the heater pulses are integrated into the unit-cell design. The placement of the switches is also shown, where GST Switches 1 are always in the same state. The substrate is a 254 µm SiC wafer, and the gold traces are 500 nm thick. The GST is simulated with extracted conductivity values from Chapter 5 with a width, length, and thickness of 30 µm, 1.3 µm, and 150 nm, respectively [153, 154].

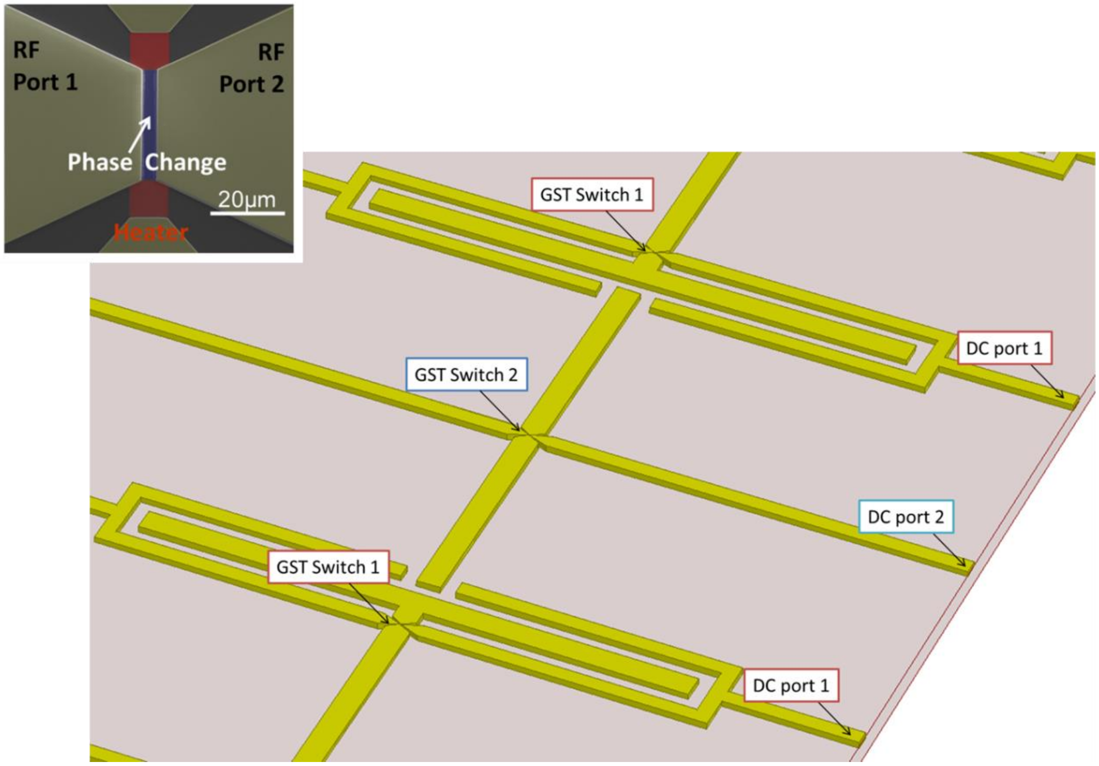

Figure 6.1. Unit-cell design with GST switches and DC heater ports designated (inset: colorized SEM of GST switch RF/heater junction [156]).

The four states of the metasurface are depicted in Figure 6.2, where green corresponds to a shorted switch and red corresponds to an open switch. The reflection curves are generated for each state from simulations of 2-D infinitely periodic arrays corresponding to each of these four switch states. From the results shown in Figure 6.3, we can see that three stationary sensing bands can be defined where each switch state corresponds to a unique presence and/or absence of reflection.

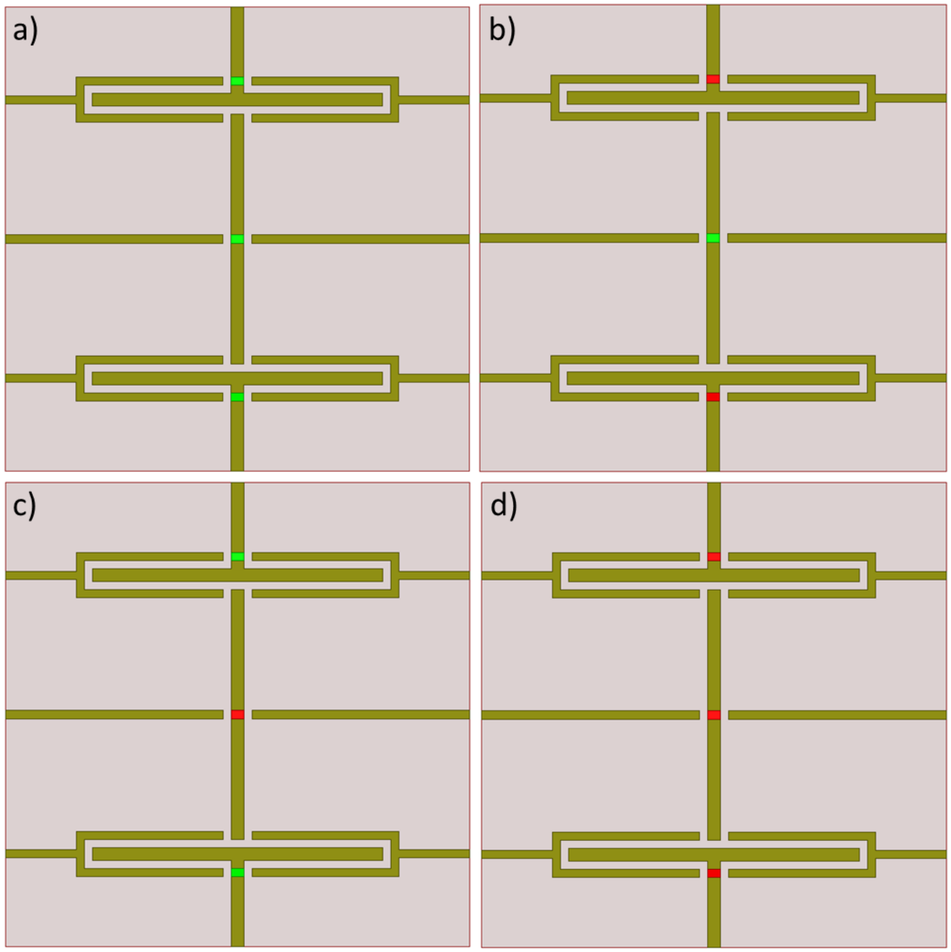

Figure 6.2. Depiction of the unit-cell with four different ideal open (red) /short (green) switch configurations.

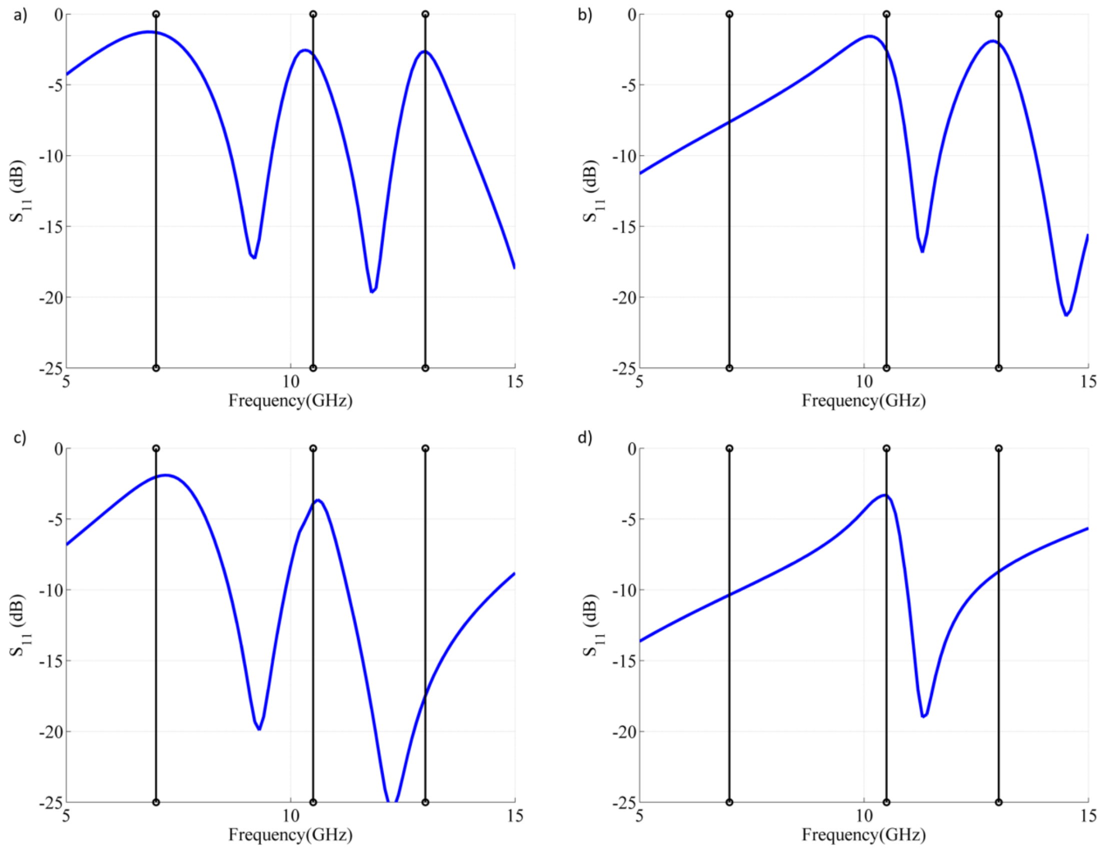

Figure 6.3. S_{11} of the different switch configurations corresponding to 2-D infinitely periodic arrays of the unit-cells from Figure 6.2.

6.1 Finite Array with DC Pulse Switching

In a practical scenario, the sensor would be deployed with a finite but usually substantial array of unit-cells. Given the need for a power source to switch the GST, a small array is desirable. Therefore, a finite array of 6 x 6 unit-cells (Figure 6.13) is simulated. For each switch configuration, the simulations for a normally incident Gaussian beam are summarized in Figure 6.14 where the off axis reflection as a function of theta is included for *bistatic* transmitter/receiver configurations. From these results, we can see that despite only utilizing a finite number of unit-cells, the array still maintains performances similar to the ones predicted by the 2-D infinitely periodic array simulations.

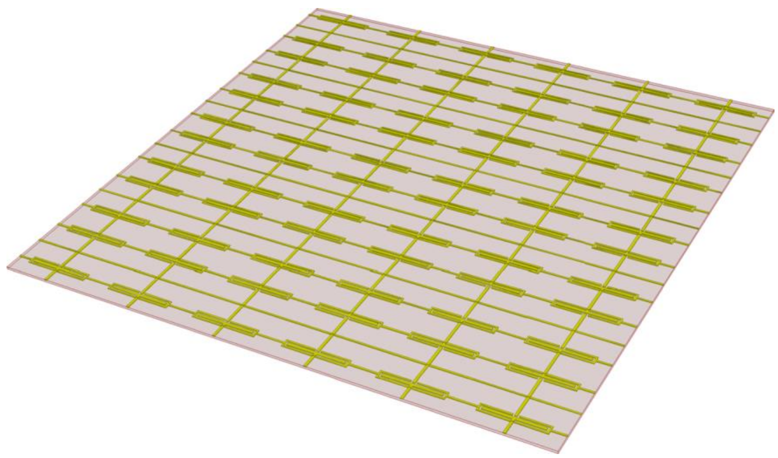

Figure 6.4. Finite 6-by-6 array of the quad state FSS geometry.

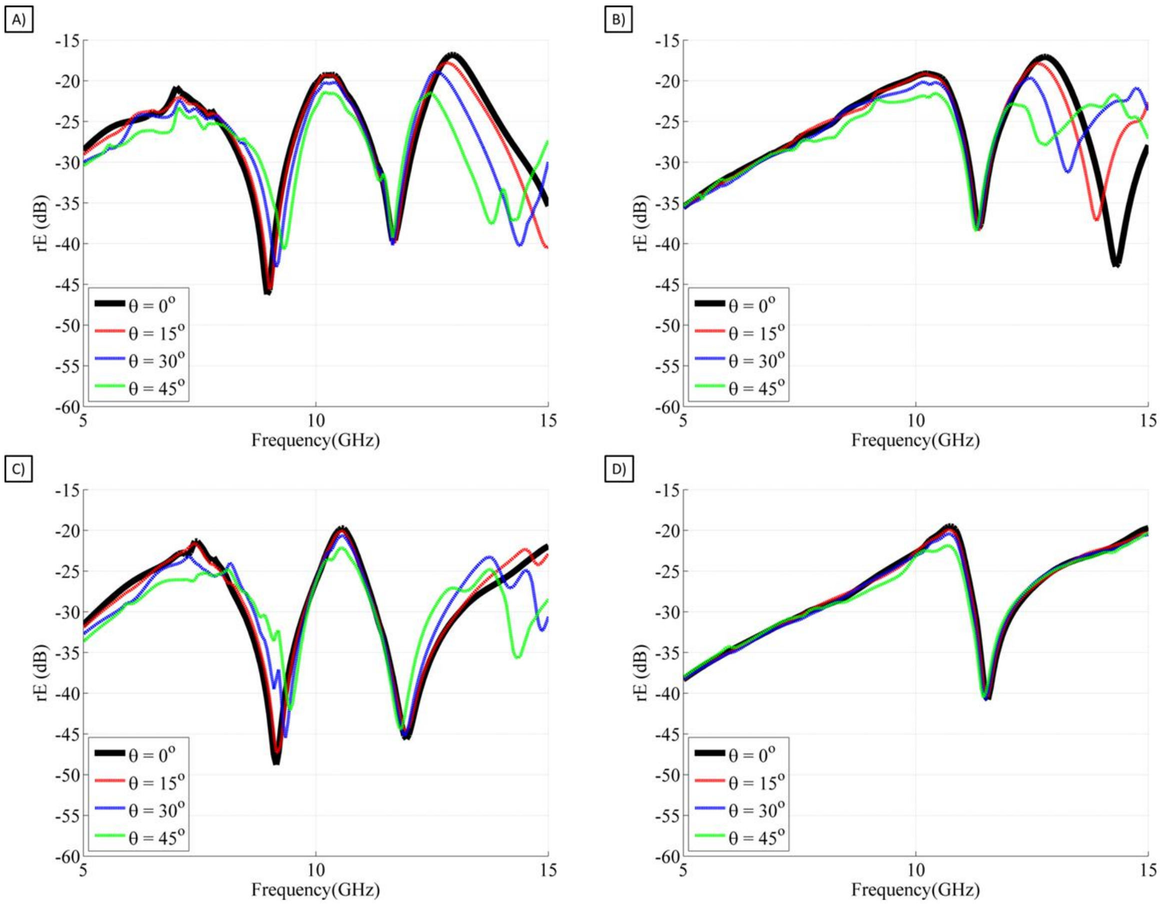

Figure 6.5. Reflection of a normally incident plane wave as a function of incidence angle reflection of the finite array depicted in Figure 6.4 with switch configurations corresponding to the switch states depicted in Figure 6.2.

Chapter 7

Conclusions and Future Work

In conclusion, several examples of novel dispersion engineered metamaterials are presented. First, the synthesized surfaces Bézier are high bandwidth wave-plates, far surpassing other know designs. Second, the composite end-load structure used to facilitate the reconfigurable microstrip patch antenna exhibits not only an intuitive easily controllable reconfigurability but also performance metrics that exceed most if not all of the conformal dual band patch antennas found in the literature. Third, the quad-state spectral bandwidth FSS demonstrates a versatile multiband reconfigurability within the X-band. In order to enable reconfigurable metamaterials at RF that exhibit a superior switching performance, the development and measurement of an RF switch chalcogenide glass phase change material is presented. The subsequent design characterization showed not only the energy saving inherent in a bistable switch but also exhibited superior performance.

Several areas of this dissertation suggest paths for further exploration:

- Broadband wave-plates may be used as signal modulators when a phase change substrate such as GST is used. If future research efforts succeed in developing a mechanism to switch this substrate phase back and forth, it could lead novel standoff detectors and communication systems which exhibit lower signal to noise ratios than intensity-based detectors.

- Metamaterial wave-plates may be implemented with antenna structures where an anisotropic ground plane can facilitate a dipole with an unbalance feed (probe feed) in addition to polarization reconfigurability.
- The Bézier synthesis technique provides a powerful new tool for the design of optimized absorbers, FSSs, emitter, modulated leaky wave antennas, metasurfaces, holographic impedance surfaces, and other applications.
- The microstrip patch antenna is the focus of future work, in so far that the design will be built and measured at the 2.4 GHz and 3.5 GHz bands. Given the frequency ratio tenability, this design approach is directly scalable to military GPS technology.
- The patch antenna may also facilitate active reconfigurability, the implementation of which needs further refining since bias lines must be included (a relatively straightforward task).
- The newly developed ChG PCM RF switch has been validated as a high performance switch. Further work now needs to determine the trade-offs between the different available ChGs. As with the case of GST and GeTe, different melting points result in slightly different energy consumption; yet, an optimal choice has yet to be agreed upon. Additionally, the thermodynamics of the heaters need to be investigated more thoroughly, as any inefficiency in the Joule heating of the PCM directly result in a need for higher switching currents and longer pulse durations. Lastly, the

ability to package an RF PCM switch compatible with PCB fabrication techniques would facilitate wide spread adoption.

- The quad-state FSS spectral barcode is a powerful design whose behavior has not yet been described in the literature. Fabrication and measurements of such a device should prove useful for stand-off detection applications.

References

1. Veselago, Victor G.. "The electrodynamics of substances with simultaneously negative value of ε and μ," Sov. Phys. Usp. **10**(4) (1968): 509–514.
2. Pendry, John B., et al. "Magnetism from conductors and enhanced nonlinear phenomena." *Microwave Theory and Techniques, IEEE Transactions on* 47.11 (1999): 2075-2084.
3. Pendry, John B. "Negative refraction makes a perfect lens." *Physical review letters* 85.18 (2000): 3966.
4. Alù, Andrea, and Nader Engheta. "Achieving transparency with plasmonic and metamaterial coatings." *Physical Review E* 72.1 (2005): 016623.
5. Pendry, John B., David Schurig, and David R. Smith. "Controlling electromagnetic fields." science 312.5781 (2006): 1780-1782.
6. Smith, David R., et al. "Composite medium with simultaneously negative permeability and permittivity." *Physical review letters* 84.18 (2000): 4184.
7. Shelby, Richard A., David R. Smith, and Seldon Schultz. "Experimental verification of a negative index of refraction." *science* 292.5514 (2001): 77-79.
8. Houck, Andrew A., Jeffrey B. Brock, and Isaac L. Chuang. "Experimental observations of a left-handed material that obeys Snell's law." *Physical Review Letters* 90.13 (2003): 137401.

9. Grbic, Anthony, and George V. Eleftheriades. "Overcoming the diffraction limit with a planar left-handed transmission-line lens." *Physical Review Letters* 92.11 (2004): 117403.

10. Schurig, David, et al. "Metamaterial electromagnetic cloak at microwave frequencies." *Science* 314.5801 (2006): 977-980.

11. Munk, Ben A. *Frequency selective surfaces: theory and design*. John Wiley & Sons, 2005.

12. Kong, Jin Au. *Electromagnetic Wave Theory* (Wiley, 1986).

13. Movchan, A. B., and S. Guenneau. "Split-ring resonators and localized modes." *Physical Review B* 70.12 (2004): 125116.

14. Caloz, Christophe, and Tatsuo Itoh. *Electromagnetic metamaterials: transmission line theory and microwave applications*. John Wiley & Sons, 2005.

15. Balanis, Constantine A. *Advanced engineering electromagnetics*. Vol. 20. New York: Wiley, 1989.

16. Hand, Thomas H. *Design and applications of frequency tunable and reconfigurable metamaterials*. Diss. DUKE UNIVERSITY, 2009.

17. Pozar, David M. *Microwave engineering*. John Wiley & Sons, 2009.

18. Sarabandi, Kamal, and Nader Behdad. "A frequency selective surface with miniaturized elements." *Antennas and Propagation, IEEE Transactions on*55.5 (2007): 1239-1245.

19. Behdad, Nader. "A second-order band-pass frequency selective surface using nonresonant subwavelength periodic structures." *Microwave and Optical Technology Letters* 50.6 (2008): 1639-1643.

20. Salehi, Mohsen, and Nader Behdad. "A second-order dual X-/Ka-band frequency selective surface."*Microwave and Wireless Components Letters, IEEE*18.12 (2008): 785-787.

21. Behdad, Nader, Mudar Al-Joumayly, and Mohsen Salehi. "A low-profile third-order bandpass frequency selective surface." *Antennas and Propagation, IEEE Transactions on* 57.2 (2009): 460-466.

22. Al-Joumayly, Mudar A., and Nader Behdad. "A generalized method for synthesizing low-profile, band-pass frequency selective surfaces with non-resonant constituting elements." *Antennas and Propagation, IEEE Transactions on* 58.12 (2010): 4033-4041.

23. Behdad, Nader, and Mudar A. Al-Joumayly. "A generalized synthesis procedure for low-profile, frequency selective surfaces with odd-order bandpass responses." *Antennas and Propagation, IEEE Transactions on* 58.7 (2010): 2460-2464.

24. Al-Joumayly, Mudar A., and Nader Behdad. "Low-profile, highly-selective, dual-band frequency selective surfaces with closely spaced bands of operation." *Antennas and Propagation, IEEE Transactions on* 58.12 (2010): 4042-4050.

25. Sievenpiper, Dan, et al. "High-impedance electromagnetic surfaces with a forbidden frequency band." *Microwave Theory and Techniques, IEEE Transactions on* 47.11 (1999): 2059-2074.

26. Lai, Anthony, Tatsuo Itoh, and Christope Caloz. "Composite right/left-handed transmission line metamaterials." *Microwave Magazine, IEEE* 5.3 (2004): 34-50.

27. Yang, Fan, and Yahya Rahmat-Samii. "Microstrip antennas integrated with electromagnetic band-gap (EBG) structures: A low mutual coupling design for array applications." *Antennas and Propagation, IEEE Transactions on* 51.10 (2003): 2936-2946.

28. Bossard, Jeremy A., Zikri Bayraktar, and Douglas H. Werner. "Broadband absorbers for the mid-IR based on multi-screen frequency selective surfaces."*Antennas and Propagation Society International Symposium (APSURSI), 2012 IEEE*. IEEE, 2012.

29. Zadeh, A. Kazem, and Anders Karlsson. "Capacitive circuit method for fast and efficient design of wideband radar absorbers." *Antennas and Propagation, IEEE Transactions on* 57.8 (2009): 2307-2314.

30. Wang, Xiande, and Douglas H. Werner. "Multiband ultra-thin electromagnetic band-gap and double-sided wideband absorbers based on resistive frequency selective surfaces." *Antennas and Propagation Society International Symposium, 2009. APSURSI'09. IEEE*. IEEE, 2009.

31. Engheta, Nader. "Thin absorbing screens using metamaterial surfaces."*Antennas and Propagation Society International Symposium, 2002. IEEE*. Vol. 2. IEEE, 2002.

32. Kern, Douglas. J., and Douglas. H. Werner. "A genetic algorithm approach to the design of ultra-thin electromagnetic bandgap absorbers." *Microwave and Optical Technology Letters* 38.1 (2003): 61-64.

33. Mosallaei, Hossein, and Kamal Sarabandi. "A one-layer ultra-thin meta-surface absorber." *Antennas and Propagation Society International Symposium, 2005 IEEE*. Vol. 1. IEEE, 2005.

34. Goldberg, David E., and John H. Holland. "Genetic algorithms and machine learning." *Machine learning* 3.2 (1988): 95-99.

35. Haupt, Randy L. "An introduction to genetic algorithms for electromagnetics."*Antennas and Propagation Magazine, IEEE* 37.2 (1995): 7-15.

36. Johnson, J. Michael, and V. Rahmat-Samii. "Genetic algorithms in engineering electromagnetics." *Antennas and Propagation Magazine, IEEE* 39.4 (1997): 7-21.

37. Weile, Daniel S., and Eric Michielssen. "Genetic algorithm optimization applied to electromagnetics: A review." *Antennas and Propagation, IEEE Transactions on* 45.3 (1997): 343-353.

38. Rahmat-Samii, Yahya, and Eric Michielssen. *Electromagnetic optimization by genetic algorithms*. John Wiley & Sons, Inc., 1999.

39. Haupt, Randy L., and Douglas H. Werner. *Genetic algorithms in electromagnetics*. John Wiley & Sons, 2007.

40. Jiang, Zhi Hao, et al. "Conformal dual-band near-perfectly absorbing mid-infrared metamaterial coating." *ACS nano* 5.6 (2011): 4641-4647.

41. Bossard, Jeremy A., et al. "Near-ideal optical metamaterial absorbers with super-octave bandwidth." *ACS nano* 8.2 (2014): 1517-1524.

42. Hansen, Nikolaus, Sibylle Müller, and Petros Koumoutsakos. "Reducing the time complexity of the derandomized evolution strategy with covariance matrix adaptation (CMA-ES)." *Evolutionary Computation* 11.1 (2003): 1-18.

43. Gregory, Micah D., Zikri Bayraktar, and Douglas H. Werner. "Fast optimization of electromagnetic design problems using the covariance matrix adaptation evolutionary strategy." *Antennas and Propagation, IEEE Transactions on* 59.4 (2011): 1275-1285.

44. Pozar, David M., and Sean M. Duffy. "A dual-band circularly polarized aperture-coupled stacked microstrip antenna for global positioning satellite." *Antennas and Propagation, IEEE Transactions on* 45.11 (1997): 1618-1625.

45. Hoorfar, Ahmad, G. Girard, and A. Perrotta. "Dual frequency circularly-polarised proximity-fed microstrip antenna." *Electronics Letters* 35.10 (1999): 759-761.

46. Laheurte, Jean-Marc. "Dual-frequency circularly polarized antennas based on stacked monofilar square spirals." *Antennas and Propagation, IEEE Transactions on*51.3 (2003): 488-492.

47. Lau, Ka-Leung, and Kwai-Man Luk. "A wide-band circularly polarized L-probe coupled patch antenna for dual-band operation." *Antennas and Propagation, IEEE Transactions on* 53.8 (2005): 2636-2644.

48. Zhou, Yijun, Chi-Chih Chen, and John L. Volakis. "Dual band proximity-fed stacked patch antenna for tri-band GPS applications." *Antennas and Propagation, IEEE Transactions on* 55.1 (2007): 220-223.

49. Chen, Zhi Ning, and Xianming Qing. "Dual-band circularly polarized-shaped slotted patch antenna with a small frequency-ratio." *Antennas and Propagation, IEEE Transactions on* 58.6 (2010): 2112-2115.

50. Sun, Xiaoye, Zhijun Zhang, and Zhenghe Feng. "Dual-band circularly polarized stacked annular-ring patch antenna for GPS application." *Antennas and Wireless Propagation Letters, IEEE* 10 (2011): 49-52.

51. Chang, The-Nan, and Jyun-Ming Lin. "Serial aperture-coupled dual band circularly polarized antenna." *Antennas and Propagation, IEEE Transactions on* 59.6 (2011): 2419-2423.

52. Chen, Can-Hui, and E. K. N. Yung. "A novel unidirectional dual-band circularly-polarized patch antenna." *Antennas and Propagation, IEEE Transactions on* 59.8 (2011): 3052-3057.

53. Jung, Youn-Kwon, and Bomson Lee. "Dual-band circularly polarized microstrip RFID reader antenna using metamaterial branch-line coupler." *Antennas and Propagation, IEEE Transactions on* 60.2 (2012): 786-791.

54. Maqsood, Mozam, et al. "A compact multipath mitigating ground plane for multiband GNSS antennas." *IEEE Transactions on Antennas and Propagation* 61.5 (2013): 2775-2782.

55. Lee, Kai Fong, and Kwai Man Luk. *Microstrip patch antennas*. Vol. 1. London: Imperial College Press, 2011.

56. Hsieh, Gui-Bin, Ming-Huang Chen, and Kin-Lu Wong. "Single-feed dual-band circularly polarised microstrip antenna." *Electronics Letters* 34.12 (1998): 1170-1171.

57. Yang, Kai-Ping, and Kin-Lu Wong. "Dual-band circularly-polarized square microstrip antenna." *Antennas and Propagation, IEEE Transactions on* 49.3 (2001): 377-382.

58. Row, J-S. "Dual-frequency circularly polarised annular-ring microstrip antenna."*Electronics Letters* 40.3 (2004): 153-154.

59. Kim, S. M., K. S. Yoon, and W. G. Yang. "Dual-band circular polarization square patch antenna for GPS and DMB." *Microwave and optical technology letters* 49.12 (2007): 2925-2926.

60. Bao, X. L., and M. J. Ammann. "Dual-frequency circularly-polarized patch antenna with compact size and small frequency ratio." *Antennas and Propagation, IEEE Transactions on* 55.7 (2007): 2104-2107.

61. Sun, Xu-Bao. "Circular-slotted microstrip antenna for GPS." *Microwave and Optical Technology Letters* 52.5 (2010): 999-1000.

62. Gaffar, Md, et al. "Design and optimisation of a novel dual-band circularly polarised microstrip antenna." *IET microwaves, antennas & propagation* 5.14 (2011): 1670-1674.

63. Sieber, Peter E., and Douglas H. Werner. "Reconfigurable broadband infrared circularly polarizing reflectors based on phase changing birefringent metasurfaces."*Optics express* 21.1 (2013): 1087-1100.

64. Sieber, Peter E., and Douglas H. Werner. "Infrared broadband quarter-wave and half-wave-plates synthesized from anisotropic Bézier metasurfaces." *Optics express* 22.26 (2014): 32371-32383.

65. Lerner, David S. "A wave polarization converter for circular polarization."*Antennas and Propagation, IEEE Transactions on* 13.1 (1965): 3-7.

66. Kärkkäinen, K., and M. Stuchly. "Frequency selective surface as a polarisation transformer." *IEE Proceedings-Microwaves, Antennas and Propagation* 149.5 (2002): 248-252.

67. Euler, M., et al. "325 GHz single layer sub-millimeter wave FSS based split slot ring linear to circular polarization convertor." *Antennas and Propagation, IEEE Transactions on* 58.7 (2010): 2457-2459.

68. Hao, Jiaming, et al. "Manipulating electromagnetic wave polarizations by anisotropic metamaterials." *Physical review letters* 99.6 (2007): 063908.

69. Strikwerda, Andrew C., et al. "Comparison of birefringent electric split-ring resonator and meanderline structures as quarter-wave-plates at terahertz frequencies." *Optics Express* 17.1 (2009): 136-149.

70. Zhao, Yang, and Andrea Alu. "Manipulating light polarization with ultrathin plasmonic metasurfaces." *Physical Review B* 84.20 (2011): 205428.

71. Yu, Nanfang, et al. "Light propagation with phase discontinuities: generalized laws of reflection and refraction." *science* 334.6054 (2011): 333-337.

72. Sun, Shulin, et al. "High-efficiency broadband anomalous reflection by gradient meta-surfaces." *Nano letters* 12.12 (2012): 6223-6229.

73. Ni, Xingjie, et al. "Broadband light bending with plasmonic nanoantennas." *Science* 335.6067 (2012): 427-427.

74. Genevet, Patrice, et al. "Ultra-thin plasmonic optical vortex plate based on phase discontinuities." *Applied Physics Letters* 100.1 (2012): 013101.

75. Khanikaev, Alexander B., et al. "Electromagnetically induced polarization conversion." *Optics Communications* 285.16 (2012): 3423-3427.

76. Doumanis, Efstratios, et al. "Anisotropic impedance surfaces for linear to circular polarization conversion." *Antennas and Propagation, IEEE Transactions on* 60.1 (2012): 212-219.

77. Pors, Anders, et al. "Broadband focusing flat mirrors based on plasmonic gradient metasurfaces." *Nano letters* 13.2 (2013): 829-834.

78. Zhao, Yang, and Andrea Alù. "Tailoring the dispersion of plasmonic nanorods to realize broadband optical meta-waveplates." *Nano letters* 13.3 (2013): 1086-1091.

79. Kildishev, Alexander V., Alexandra Boltasseva, and Vladimir M. Shalaev. "Planar photonics with metasurfaces." *Science* 339.6125 (2013): 1232009.

80. Pors, Anders, et al. "Gap plasmon-based metasurfaces for total control of reflected light." *Scientific reports* 3 (2013).

81. Pors, Anders, Michael G. Nielsen, and Sergey I. Bozhevolnyi. "Broadband plasmonic half-wave-plates in reflection." *Optics letters* 38.4 (2013): 513-515.

82. Lévesque, Quentin, et al. "Plasmonic planar antenna for wideband and efficient linear polarization conversion." *Applied Physics Letters* 104.11 (2014): 111105.

83. Wang, Yanqin, et al. "Dynamic manipulation of polarization states using anisotropic meta-surface." *Optics Communications* 319 (2014): 14-16.

84. Jiang, Shang-Chi, et al. "Controlling the polarization state of light with a dispersion-free metastructure." *Physical Review X* 4.2 (2014): 021026.

85. Ma, Hui Feng, et al. "Broadband circular and linear polarization conversions realized by thin birefringent reflective metasurfaces." *Optical Materials Express*4.8 (2014): 1717-1724.

86. Veysi, Mehdi, et al. "Thin anisotropic metasurfaces for simultaneous light focusing and polarization manipulation." *JOSA B* 32.2 (2015): 318-323.

87. Peralta, Xomalin G., et al. "Metamaterials for THz polarimetric devices." *Optics express* 17.2 (2009): 773-783.

88. Chin, Jessie Y., et al. "An efficient broadband metamaterial wave retarder." *Optics express* 17.9 (2009): 7640-7647.

89. Hao, Jiaming, et al. "Optical metamaterial for polarization control." *Physical Review A* 80.2 (2009): 023807.

90. Hao, Jia-ming, Min Qiu, and Lei Zhou. "Manipulate light polarizations with metamaterials: From microwave to visible." *Frontiers of physics in China* 5 (2010): 291-307.

91. Liu, Mingkai, et al. "Incident-angle-insensitive and polarization independent polarization rotator." *Optics express* 18.11 (2010): 11990-12001.

92. Li, Zhancheng, et al. "High Performance Broadband Asymmetric Polarization Conversion Due to Polarization-dependent Reflection." *Plasmonics* (2015): 1-9.

93. Orfanidis, Sophocles J. *Electromagnetic waves and antennas*. New Brunswick, NJ: Rutgers University, 2002.

94. Heidari, Abbas Ali, Mohammad Heyrani, and Mansoor Nakhkash. "A dual-band circularly polarized stub loaded microstrip patch antenna for GPS applications." *Progress In Electromagnetics Research* 92 (2009): 195-208.

95. Hasan, Md Nazmul, et al. "Design and simulation based studies of a dual band u-slot patch antenna for WLAN application." *Advanced Communication Technology (ICACT), 2012 14th International Conference on*. IEEE, 2012.

96. Al-Joumayly, Mudar, et al. "Dual-band miniaturized patch antennas for microwave breast imaging." *Antennas and Wireless Propagation Letters, IEEE*9 (2010): 268-271.

97. Maci, S., et al. "Dual-band slot-loaded patch antenna." *Microwaves, Antennas and Propagation, IEE Proceedings*. Vol. 142. No. 3. IET, 1995.

98. Lee, Kai F., et al. "On the use of U-slots in the design of dual-and triple-band patch antennas." *Antennas and Propagation Magazine, IEEE* 53.3 (2011): 60-74.

99. Oliveri, Giacomo, Douglas H. Werner, and Andrea Massa. "Reconfigurable Electromagnetics Through Metamaterials—A Review." (2015).

100. Ourir, A., S. N. Burokur, and Andre de Lustrac. "Electronically reconfigurable metamaterial for compact directive cavity antennas." *Electronics Letters* 43.13 (2007): 698-700.

101. Mirzaei, Hassan, and George V. Eleftheriades. "A compact frequency-reconfigurable metamaterial-inspired antenna." *Antennas and Wireless Propagation Letters, IEEE* 10 (2011): 1154-1157.

102. Burokur, Shah Nawaz, et al. "Low-profile frequency agile directive antenna based on an active metasurface." *Microwave and Optical Technology Letters*53.10 (2011): 2291-2295.

103. Tang, Junyan, et al. "A continuously tunable miniaturized patch antenna."*Antennas and Wireless Propagation Letters, IEEE* 13 (2014): 1080-1083.

104. White, Carson R., and Gabriel M. Rebeiz. "Single-and dual-polarized tunable slot-ring antennas." *Antennas and Propagation, IEEE Transactions on* 57.1 (2009): 19-26.

105. Behdad, Nader, and Kamal Sarabandi. "A varactor-tuned dual-band slot antenna." *Antennas and Propagation, IEEE Transactions on* 54.2 (2006): 401-408.

106. Behdad, Nader, and Kamal Sarabandi. "Dual-band reconfigurable antenna with a very wide tunability range." *Antennas and Propagation, IEEE Transactions on*54.2 (2006): 409-416.

107. Mias, Christos, and Jyh Haur Yap. "A varactor-tunable high impedance surface with a resistive-lumped-element biasing grid." *Antennas and Propagation, IEEE Transactions on* 55.7 (2007): 1955-1962.

108. Bayatpur, Farhad, and Kamal Sarabandi. "A tunable metamaterial frequency-selective surface with variable modes of operation." *Microwave Theory and Techniques, IEEE Transactions on* 57.6 (2009): 1433-1438.

109. Burokur, S. N., et al. "Tunable bilayered metasurface for frequency reconfigurable directive emissions." *Applied Physics Letters* 97.6 (2010): 064101.

110. Jiang, Tao, et al. "Low-DC voltage-controlled steering-antenna radome utilizing tunable active metamaterial." *Microwave Theory and Techniques, IEEE Transactions on* 60.1 (2012): 170-178.

111. Tang, Junyan, et al. "A continuously tunable miniaturized patch antenna. "*Antennas and Wireless Propagation Letters, IEEE* 13 (2014): 1080-1083.

112. Sheta, Abdel-Fattah, and Samir F. Mahmoud. "A widely tunable compact patch antenna." *Antennas and Wireless Propagation Letters, IEEE* 7 (2008): 40-42.

113. Li, Hui, et al. "A simple compact reconfigurable slot antenna with a very wide tuning range." *Antennas and Propagation, IEEE Transactions on* 58.11 (2010): 3725-3728.

114. Niroo-Jazi, Mahmoud, and Tayeb Denidni. "Reconfigurable dual-band frequency selective surfaces using a new hybrid element." *Antennas and Propagation (APSURSI), 2011 IEEE International Symposium on*. IEEE, 2011.

115. Rebeiz, Gabriel M., and Jeremy B. Muldavin. "RF MEMS switches and switch circuits." *Microwave Magazine, IEEE* 2.4 (2001): 59-71.

116. Turpin, Jeremiah P., et al. "Reconfigurable and tunable metamaterials: a review of the theory and applications." *International Journal of Antennas and Propagation* 2014 (2014).

117. Ho, Kevin Ming-Jiang, and Gabriel M. Rebeiz. "Microstrip antennas with full polarization diversity using packaged RF MEMS switches." *Antennas and Propagation Society International Symposium (APSURSI), 2012 IEEE*. IEEE, 2012.

118. Zohur, Abdul, et al. "RF MEMS reconfigurable two-band antenna." *Antennas and Wireless Propagation Letters, IEEE* 12 (2013): 72-75.

119. Rajagopalan, Harish, Joshua M. Kovitz, and Yahya Rahmat-Samii. "MEMS reconfigurable optimized e-shaped patch antenna design for cognitive radio."*Antennas and Propagation, IEEE Transactions on* 62.3 (2014): 1056-1064.

120. Jung, Tony J., et al. "Circular/linear polarization reconfigurable antenna on simplified RF-MEMS packaging platform in K-band." *Antennas and Propagation, IEEE Transactions on* 60.11 (2012): 5039-5045.

121. Debogovic, Tomislav, Juraj Bartolic, and Julien Perruisseau-Carrier. "Dual-polarized partially reflective surface antenna with MEMS-based beamwidth reconfiguration." *Antennas and Propagation, IEEE Transactions on* 62.1 (2014): 228-236.

122. Schoenlinner, Bernhard, Leo C. Kempel, and Gabriel M. Rebeiz. "Switchable RF MEMS Ka-band frequency-selective surface." *Microwave Symposium Digest, 2004 IEEE MTT-S International*. Vol. 2. IEEE, 2004.

123. Coutts, G. M., R. R. Mansour, and S. K. Chaudhuri. "A MEMS-tunable frequency-selective surface monolithically integrated on a flexible substrate."*Microwave Symposium, 2007. IEEE/MTT-S International*. IEEE, 2007.

124. Chan, King Yuk, and Y. Jay Guo. "Analysis of RF MEMS integrated tunable high impedance surface at 60 GHz." *Microwave Conference Proceedings (APMC), 2011 Asia-Pacific*. IEEE, 2011.

125. Kiani, Ghaffer, Trevor S. Bird, and King Y. Chan. "MEMS enabled frequency selective surface for 60 GHz applications." *Antennas and Propagation (APSURSI), 2011 IEEE International Symposium on*. IEEE, 2011.

126. Safari, Majid, Cyrus Shafai, and Lotfollah Shafai. "Development of a MEMS-enabled frequency selective surface." *Antenna Technology and Applied Electromagnetics (ANTEM), 2014 16th International Symposium on*. IEEE, 2014.

127. Safari, Mojtaba, Cyrus Shafai, and Lotfollah Shafai. "X-Band Tunable Frequency Selective Surface Using MEMS Capacitive Loads." *Antennas and Propagation, IEEE Transactions on* 63.3 (2015): 1014-1021.

128. Debogovic, Tomislav, and Julien Perruisseau-Carrier. "MEMS-reconfigurable metamaterials and antenna applications." *International Journal of Antennas and Propagation* 2014 (2014).

129. Hand, Thomas, and Steven Cummer. "Characterization of tunable metamaterial elements using MEMS switches." *Antennas and Wireless Propagation Letters, IEEE* 6 (2007): 401-404.

130. Schoenlinner, Bernhard, et al. "Switchable low-loss RF MEMS Ka-band frequency-selective surface." *Microwave Theory and Techniques, IEEE Transactions on* 52.11 (2004): 2474-2481.

131. Sanz-Izquierdo, Benito, and Edward Parker. "Dual polarized reconfigurable frequency selective surfaces." *Antennas and Propagation, IEEE Transactions on* 62.2 (2014): 764-771.

132. Bayatpur, Farhad, and Kamal Sarabandi. "Design and analysis of a tunable miniaturized-element frequency-selective surface without bias network."*Antennas and Propagation, IEEE Transactions on* 58.4 (2010): 1214-1219.

133. Bayatpur, Farhad, and Kamal Sarabandi. "A tunable metamaterial frequency-selective surface with variable modes of operation." *Microwave Theory and Techniques, IEEE Transactions on* 57.6 (2009): 1433-1438.

134. Grant, P. D., M. W. Denhoff, and R. R. Mansour. "A comparison between RF MEMS switches and semiconductor switches." *MEMS, NANO and Smart Systems, 2004. ICMENS 2004. Proceedings. 2004 International Conference on*. IEEE, 2004.

135. Werner, Douglas H., Theresa S. Mayer, and Peter E. Sieber. "Radio frequency switch and processes of selectively regulating radio frequency energy transmission." U.S. Patent Application 14/205,640.

136. Sieber, Peter E., and Douglas H. Werner. "A reconfigurable dual-band circularly polarizing miniaturized conformal patch antenna exhibiting small frequency

ratios." *Antennas and Propagation Society International Symposium (APSURSI), 2014 IEEE*. IEEE, 2014.

137. Sieber, Peter E., and Douglas H. Werner. "Reconfigurable broadband infrared circularly polarizing anisotropic impedance surfaces synthesised via Bézier surfaces." *Antennas and Propagation Society International Symposium (APSURSI), 2014 IEEE*. IEEE, 2014.

138. Sieber, Peter E., and Douglas H. Werner. "Reconfigurable broadband infrared circularly polarizing reflectors based on phase changing birefringent metasurfaces."*Optics express* 21.1 (2013): 1087-1100.

139. Farouki, Rida T. "The Bernstein polynomial basis: a centennial retrospective."*Computer Aided Geometric Design* 29.6 (2012): 379-419.

140. Raoux, Simone, and Matthias Wuttig, eds. *Phase change materials: science and applications*. Springer Science & Business Media, 2010.

141. Ovshinsky, Stanford R. "Reversible electrical switching phenomena in disordered structures." *Physical Review Letters* 21.20 (1968): 1450.

142. Avrami, Melvin. "Kinetics of phase change. I General theory." *The Journal of Chemical Physics* 7.12 (1939): 1103-1112.

143. Weiser, K., R. J. Gambino, and J. A. Reinhold. "Laser-beam writing on amorphous chalcogenide films: crystallization kinetics and analysis of amorphizing energy." *Applied Physics Letters* 22.1 (1973): 48-49.

144. Lacaita, A. L., et al. "Electrothermal and phase-change dynamics in chalcogenide-based memories." *Electron Devices Meeting, 2004. IEDM Technical Digest. IEEE International*. IEEE, 2004.

145. Hudgens, Stephen, and Brian Johnson. "Overview of phase-change chalcogenide nonvolatile memory technology." *MRS bulletin* 29.11 (2004): 829-832.

146. Redaelli, A., et al. "Electronic switching effect and phase-change transition in chalcogenide materials." *IEEE Electron Device Letters* 25.10 (2004): 684-686.

147. Ielmini, D., et al. "Assessment of threshold switching dynamics in phase-change chalcogenide memories." *Electron Devices Meeting, 2005. IEDM Technical Digest. IEEE International*. IEEE, 2005.

148. Driscoll, Tom, et al. "Dynamic tuning of an infrared hybrid-metamaterial resonance using vanadium dioxide." *Applied Physics Letters* 93.2 (2008): 024101.

149. Fallica, Roberto, et al. "Thermal and Electrical Characterization of Materials for Phase-Change Memory Cells†." *Journal of Chemical & Engineering Data* 54.6 (2009): 1698-1701.

150. Danner, Brent L., and Ronald A. Coutu. "Characterizing Metal-Insulator-Transition (MIT) Phase Change Materials (PCM) for RF and DC Micro-switching Elements." *Procedia Engineering* 47 (2012): 80-83.

151. Rodríguez-Solís, Rafael A., Hector L. Pacheco, and Nelson Sepulveda. "Reconfigurable slotted microstrip patch using VO 2." *Proceedings of the 2012 IEEE International Symposium on Antennas and Propagation*. 2012.

152. Scott, Sean, et al. "A frequency selective surface with integrated limiter for receiver protection." *Antennas and Propagation Society International Symposium (APSURSI), 2012 IEEE*. IEEE, 2012.

153. El-Hinnawy, Nabil, et al. "A Four-Terminal, Inline, Chalcogenide Phase-Change RF Switch Using an Independent Resistive Heater for Thermal Actuation."*Electron Device Letters, IEEE* 34.10 (2013): 1313-1315.

154. El-Hinnawy, Nabil, et al. "A 7.3 THz cut-off frequency, inline, chalcogenide phase-change RF switch using an independent resistive heater for thermal actuation." *Compound Semiconductor Integrated Circuit Symposium (CSICS), 2013 IEEE*. IEEE, 2013.

155. Shim, Yonghyun, Gwendolyn Hummel, and Mina Rais-Zadeh. "RF switches using phase change materials." *Micro Electro Mechanical Systems (MEMS), 2013 IEEE 26th International Conference on*. IEEE, 2013.

156. El-Hinnawy, Nabil, et al. "Low-loss latching microwave switch using thermally pulsed non-volatile chalcogenide phase change materials." *Applied Physics Letters* 105.1 (2014): 013501.

157. Young, Robert M., et al. "Thermal analysis of an indirectly heat pulsed non-volatile phase change material microwave switch." *Journal of Applied Physics*116.5 (2014): 054504.

158. El-Hinnawy, Nabil, et al. "Improvements in GeTe-Based Inline Phase-Change Switch Technology for RF Switching Applications." *CS MANTECH Conf., May 19th-22nd*. 2014.

159. King, Matthew R., et al. "Development of cap-free sputtered GeTe films for inline phase change switch based RF circuits." *Journal of Vacuum Science & Technology B* 32.4 (2014): 041204.

160. Romeu, Jordi, and Yahya Rahmat-Samii. "Fractal FSS: A novel dual-band frequency selective surface." *Antennas and Propagation, IEEE Transactions on* 48.7 (2000): 1097-1105.

161. Gianvittorio, John P., et al. "Self-similar prefractal frequency selective surfaces for multiband and dual-polarized applications." *Antennas and Propagation, IEEE Transactions on* 51.11 (2003): 3088-3096.

162. Ohira, Masataka, et al. "Multiband single-layer frequency selective surface designed by combination of genetic algorithm and geometry-refinement technique." *Antennas and Propagation, IEEE Transactions on* 52.11 (2004): 2925-2931.

163. Kern, Douglas J., et al. "The design synthesis of multiband artificial magnetic conductors using high impedance frequency selective surfaces." *Antennas and Propagation, IEEE Transactions on* 53.1 (2005): 8-17.

164. Kim, Dong Ho, and Jae Ick Choi. "Design of a multiband frequency selective surface." *ETRI journal* 28.4 (2006): 506-508.

165. Guo, Chao, Hou-Jun Sun, and Xin Lv. "A novel dualband frequency selective surface with periodic cell perturbation." *Progress In Electromagnetics Research B* 9 (2008): 137-149.

166. Huang, Min-Jie, et al. "A new type of combined element multiband frequency selective surface." *Antennas and Propagation, IEEE Transactions on* 57.6 (2009): 1798-1803.

167. Coombs, J. H., et al. "Laser-induced crystallization phenomena in GeTe-based alloys. I. Characterization of nucleation and growth." *Journal of applied physics*78.8 (1995): 4906-4917.

168. Hurwitz, Henry, and R. Clark. Jones. "A new calculus for the treatment of optical systems I. description and discussion of the calculus." *J. Opt. Soc. Am* 31 (1941): 488-493.

VITA

Peter E. Sieber

Education

The Pennsylvania State University, University Park, PA
Ph.D. in Electrical Engineering, (8/09-8/15).

University of Wisconsin-Milwaukee, Milwaukee, WI
B.S. in Electrical Engineering, (7/06-5/09)

Select Publications and Patent

1. **P. E. Sieber** and D. H. Werner, "Infrared Broadband Quarter-wave and Half-wave-plates Synthesized from Anisotropic Bézier Metasurfaces,"*Optics Express*, Vol. 22, No. 26, pp. 32371-32383, Dec. 2014
2. **P. E. Sieber**, and D. H. Werner, "Reconfigurable Broadband Infrared Circularly Polarizing Reflectors Based on Phase Changing Birefringent Metasurfaces," Optics Express, Vol. 21, No. 1, pp. 1087-1100, 2013.
3. **P. E. Sieber**, and D. H. Werner, " A Reconfigurable Dual-band Circularly Polarizing Miniturized Conformal Patch Antenna Exhibiting Small Frequency Ratios," Proceedings of the International Symposium on Antennas and Propagation and USNC/URSI National Radio Science Meeting Memphis, TN, USA, July 6-12, 2014.
4. **P. E. Sieber**, and D. H. Werner, " Reconfigurable Broadband Infrared Circularly Polarizing Anisotropic Impedance Surfaces Synthesised via Bézier Surfaces," Proceedings of the International Symposium on Antennas and Propagation and USNC/URSI National Radio Science Meeting Memphis, TN, USA, July 6-12, 2014.
5. **P. E. Sieber**, and D. H. Werner, "A Reconfigurable Near-infrared Circularly Polarizing Reflector Based on Phase Changing Anisotropic Metamaterials," Proceedings of the International Symposium on Antennas and Propagation and USNC/URSI National Radio Science Meeting Chicago, IL, USA, July 8-14, 2012.
6. **P. E. Sieber**, M. G. Bray, J. A. Bossard, A. E. Kovalev, T. S. Mayer, and D. H. Werner, "Stand-off Detection of Chemical Analytes with Passive Chemo-Sensing IR Absorbers," Proceedings of the 2010 IEEE International Symposium on Antennas and Propagation and USNC/URSI National Radio Science Meeting, Toronto, Canada, July 11-17, 2010.
7. Werner, Douglas H., Theresa S. Mayer, and **Peter E. Sieber**. "Radio frequency switch and processes of selectively regulating radio frequency energy transmission." U.S. Patent Application 14/205,640.
8. J. P. Turpin, **P. E. Sieber**, and D. H. Werner, "Absorbing Ground Planes for Reducing Planar Antenna Radar Cross-Section Based on Frequency Selective Surfaces," IEEE Antennas and Wireless Propagation Letters Vol. 12, pp. 1456-1459, 2013.
9. J. P. Turpin, **P.E. Sieber**, and D. H. Werner, "Absorbing FSS Ground Plane for Reduced-Radar Cross Section of Conformal Antennas," Proceedings of the 2013 IEEE International Symposium on Antennas & Propagation and USNC/URSI National Radio Science Meeting, July 7-13, 2013, Orlando, FL, USA.
10. Z. H. Jiang, **P. E. Sieber**, L. Kang, and D. H. Werner, "Restoring Intrinsic Properties of Electromagnetic Radiators Using Ultra-Lightweight Integrated Metasurface Cloaks," Accepted for publication in *Advanced Functional Materials*.
11. D. E. Brocker, **P. E. Sieber**, J. A. Waynert, J. Li, P. L. Werner and D. H. Werner, "A Hybrid Approach for Efficient Modeling of Medium-Frequency Propagation in Coal Mines," *IEEE Antennas and Propagation Magazine*, Vol. 57, No. 1, pp. 1-14, Feb. 2015.